

Antarctic Sea Ice Response to Weather and Climate Modes of Variability*

TSUBASA KOHYAMA AND DENNIS L. HARTMANN

Department of Atmospheric Sciences, University of Washington, Seattle, Washington

(Manuscript received 27 April 2015, in final form 29 October 2015)

ABSTRACT

The relationship between climate modes and Antarctic sea ice is explored by separating the variability into intraseasonal, interannual, and decadal time scales. Cross-spectral analysis shows that geopotential height and Antarctic sea ice extent are most coherent at periods between about 20 and 40 days (the intraseasonal time scale). In this period range, where the atmospheric circulation and the sea ice extent are most tightly coupled, sea ice variability responds strongly to Rossby waves with the structure of the Pacific–South American (PSA) pattern. The PSA pattern in this time scale is not directly related to El Niño–Southern Oscillation (ENSO) or the southern annular mode (SAM), which have received much attention for explaining Antarctic sea ice variability. On the interannual time scale, ENSO and SAM are important, but a large fraction of sea ice variance can also be explained by Rossby wave-like structures in the Drake Passage region. After regressing out the sea ice extent variability associated with ENSO, the observed positive sea ice trends in Ross Sea and Indian Ocean during the satellite era become statistically insignificant. Regressing out SAM makes the sea ice trend in the Indian Ocean insignificant. Thus, the positive trends in sea ice in the Ross Sea and the Indian Ocean sectors may be explained by the variability and decadal trends of known interannual climate modes.

1. Introduction

Sea ice near the poles plays an integral part in Earth's climate system, including hindering the thermal interaction between atmosphere and ocean and modulating the Earth surface albedo (e.g., Parkinson and Cavalieri 2012). Its variability also has large impacts on local ecosystems (Ainley et al. 2003). The mechanisms controlling the sea ice extent (SIE) time series, shown in Fig. 1, are not yet fully understood. Many previous studies have pointed out that sea ice variability can be caused by fluctuations of the atmospheric circulation associated with intraseasonal (e.g., Renwick et al. 2012), interannual, and decadal climate variability, such as the southern annular mode (SAM) (e.g., Hall and Visbeck 2002; Lefebvre et al. 2004; Stammerjohn et al. 2008; Simpkins et al. 2012), El Niño–Southern Oscillation (ENSO) (Simmonds and Jacka 1995; Yuan 2004;

Stammerjohn et al. 2008; Simpkins et al. 2012), and the Atlantic multidecadal oscillation (AMO) (Li et al. 2014). Despite these extensive research efforts, there has been less comprehensive research to assess the relative importance of these weather and climate influences for Antarctic sea ice variability.

It is important to appreciate that atmospheric variability behaves differently for different time scales. Figure 2 shows the dominant structures of atmospheric variability in the Southern Hemisphere in the form of empirical orthogonal functions (EOFs) of 500-hPa geopotential height (Z). Unfiltered atmospheric variability (Fig. 2a) exhibits different structures from daily or weekly variability (Fig. 2b), which are dominated by weather disturbances associated with eastward-propagating Rossby waves. Another example is SAM, which is important on the interannual time scale (Fig. 2c), but not for the intraseasonal time scale. Teleconnections from the tropics, such as ENSO variability, are detectable on interannual time scales, but not on intraseasonal time scales. This is because tropical sea surface temperature (SST) is highly persistent, yet much extratropical variability occurs on shorter time scales.

We expect the atmospheric patterns that can effectively modulate sea ice to be different for different time scales. Figure 3 shows maps of Z regressed onto SIE

* Supplemental information related to this paper is available at the Journals Online website: <http://dx.doi.org/10.1175/JCLI-D-15-0301.s1>.

Corresponding author address: Tsubasa Kohyama, Department of Atmospheric Sciences, University of Washington, Box 351640, Seattle, WA 98195-1640.
E-mail: kohyama@uw.edu

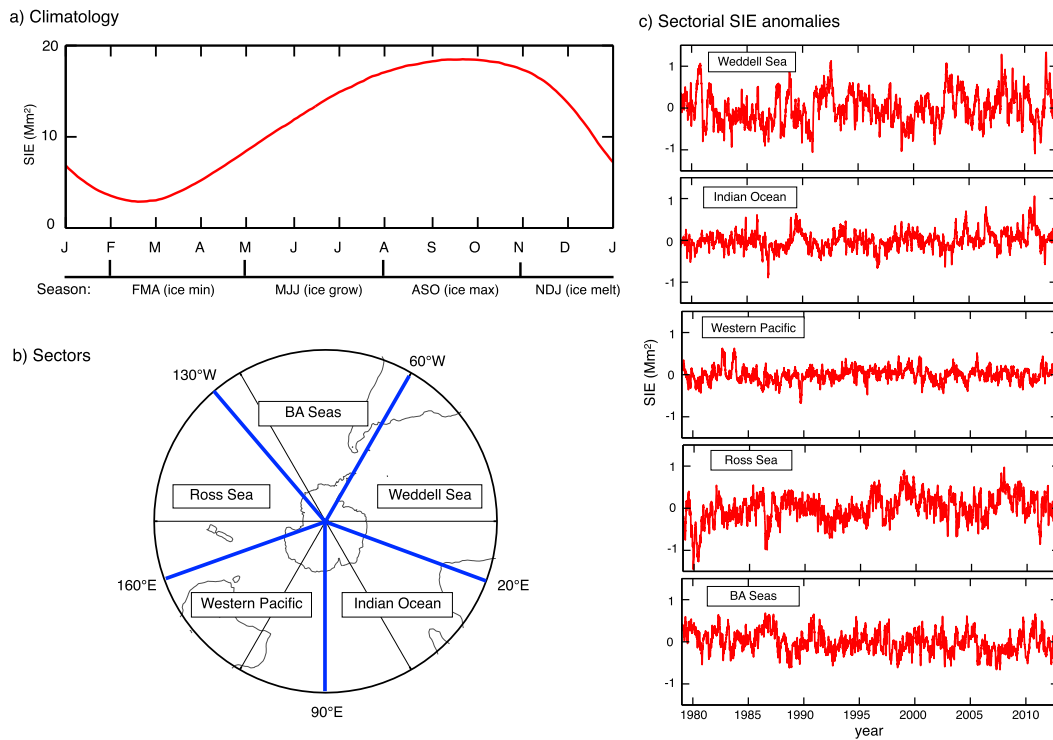


FIG. 1. (a) Climatology of the Southern Hemispheric sea ice extent (SIE) in two-day resolution. Definitions of each season used in this study are indicated below the panel. (b) Geographical description of longitudinal sectors for SIE data. Stereographic projection is used with the center at the South Pole and the 0° meridian on the right. (c) SIE anomaly (i.e., deviation from climatology) time series for each sector in 2-day resolution.

time series in each longitudinal sector for different time scales. Unfiltered data show that dipole patterns of Z modulate SIE in particular longitudinal sectors (Fig. 3a). Specifically, the dipole pattern consists of a low anomaly prevalent in the eastern half of the sector and a high anomaly in the west. Considering the geostrophic relationship, this means that the SIE increase is associated with cold southerly wind anomalies, and vice versa, which is consistent with previous studies (e.g., Lefebvre and Goosse 2005; Renwick et al. 2012; Holland and Kwok 2012). Figures 3b and 3c suggest, however, that the height patterns that yield sea ice increases depend on the time scale. Intraseasonal variability involves local weather disturbances, whereas interannual sea ice variability seems to be associated with more global structures. Here, we examine the role of climate modes for explaining Antarctic sea ice variability on different time scales.

In this study, we provide a comprehensive analysis of the effects of weather and climate variability upon Antarctic sea ice, on various time and space scales. The data used in this study are described in the following section. Next, we introduce cross-spectral analysis in section 3 to demonstrate that meteorology has the strongest linear relationship with sea ice variability for

the intraseasonal time scale. In section 4, we explore some dominant modes of intraseasonal variability in the atmosphere and compare their importances for Antarctic sea ice modulation. Then, in section 5, we extend our analysis to the interannual time scale. Section 6 gives some possible implications of our study for the observed increasing trend of Antarctic sea ice extent. Conclusions are given in section 7.

2. Data and methods

a. Data

The time span of the record analyzed in this study is from 1979 through 2012. Because the SIE dataset described in the next paragraph is given with only 2-day time resolution until the middle of 1987, we have used 2-day or monthly data unless noted otherwise. In addition, the sea ice concentration data are missing at the beginning of 1988. The analysis performed with once-daily data is thus based on the time span from 1989 through 2012.

The daily and monthly SIE data used in this study are from Antarctic sea ice time series calculated by National Aeronautics and Space Administration (NASA) Cryosphere Science Laboratory (Parkinson and Cavalieri

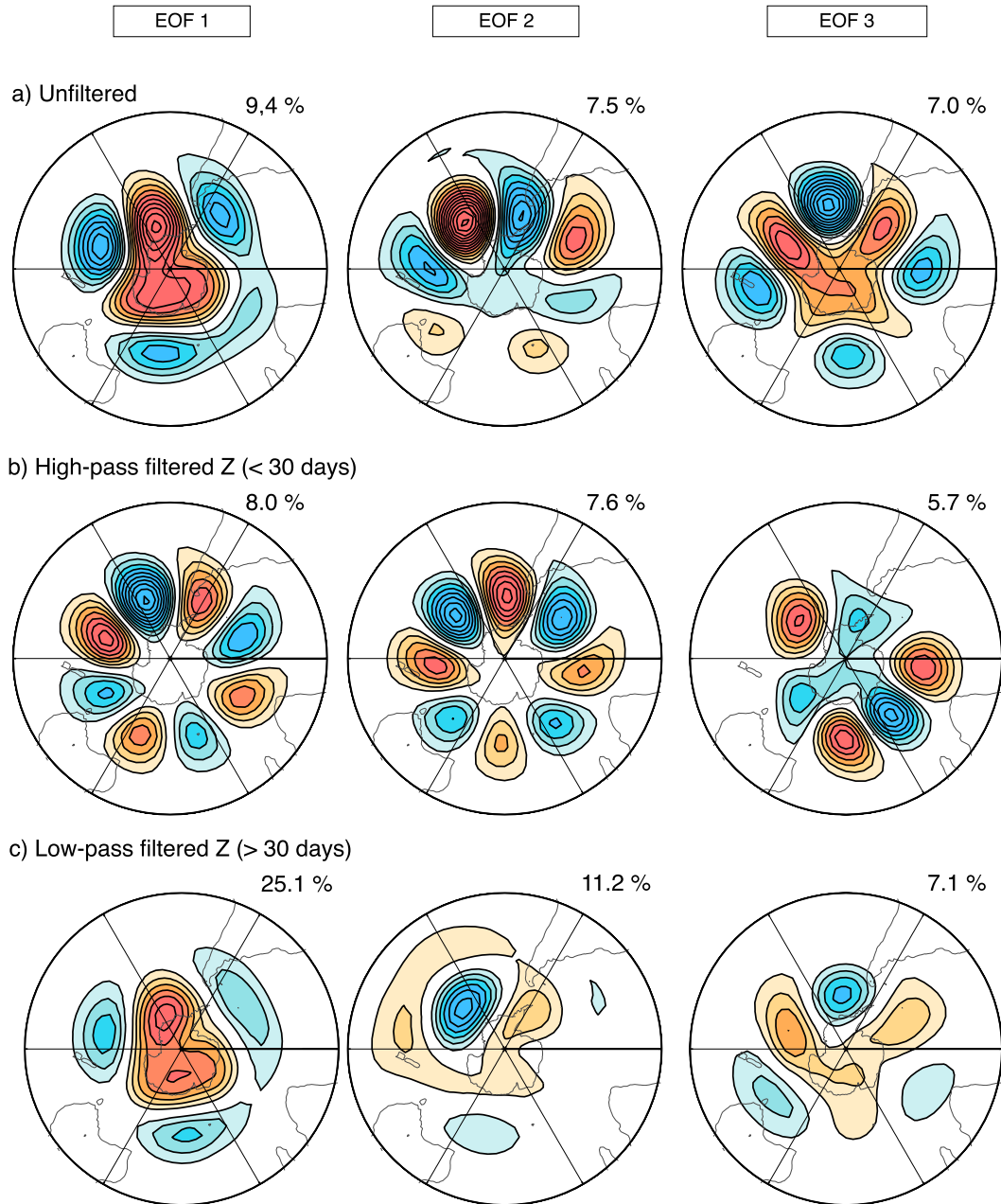


FIG. 2. (a) Regression maps of unfiltered 500-hPa geopotential height (m) onto its standardized PC1, PC2, and PC3 time series calculated for the region south of 30°S for all months. Daily climatology and linear trend are removed by regression beforehand. Contour interval is 10 m. Zero contours are omitted, and positive (negative) local maxima are shaded orange (blue). Variance contributions are indicated on top right. (b) As in (a), but for high-pass filtered 500-hPa Z for periods shorter than 30 days in period, calculated using a second-order Butterworth filter. (c) As in (b), but for low-pass filtered 500-hPa Z.

Downloaded from http://journals.ametsoc.org/jcl/article-pdf/29/2/721/4067739/jcl-d-15-0301_1.pdf by UNIVERSITY OF AUCKLAND user on 30 June 2020

2012), available online at <http://neptune.gsfc.nasa.gov/csb/index.php?section=59>. The time series are available for six different Antarctic sectors including the Weddell Sea (WS; 60°W–20°E), Indian Ocean (IO; 20°–90°E), western Pacific Ocean (WP; 90°–160°E), Ross Sea (RS; 160°E–130°W), Bellingshausen–Amundsen Seas (BA;

130°–60°W), and Southern Hemisphere (SH; all longitudes) as shown in Fig. 1b.

The daily and monthly reanalysis data including geopotential at 500 and 1000 hPa, meridional wind (v) and temperature (T) at 1000 hPa, and SST are from the four-times-daily ERA-Interim reanalysis data (Dee

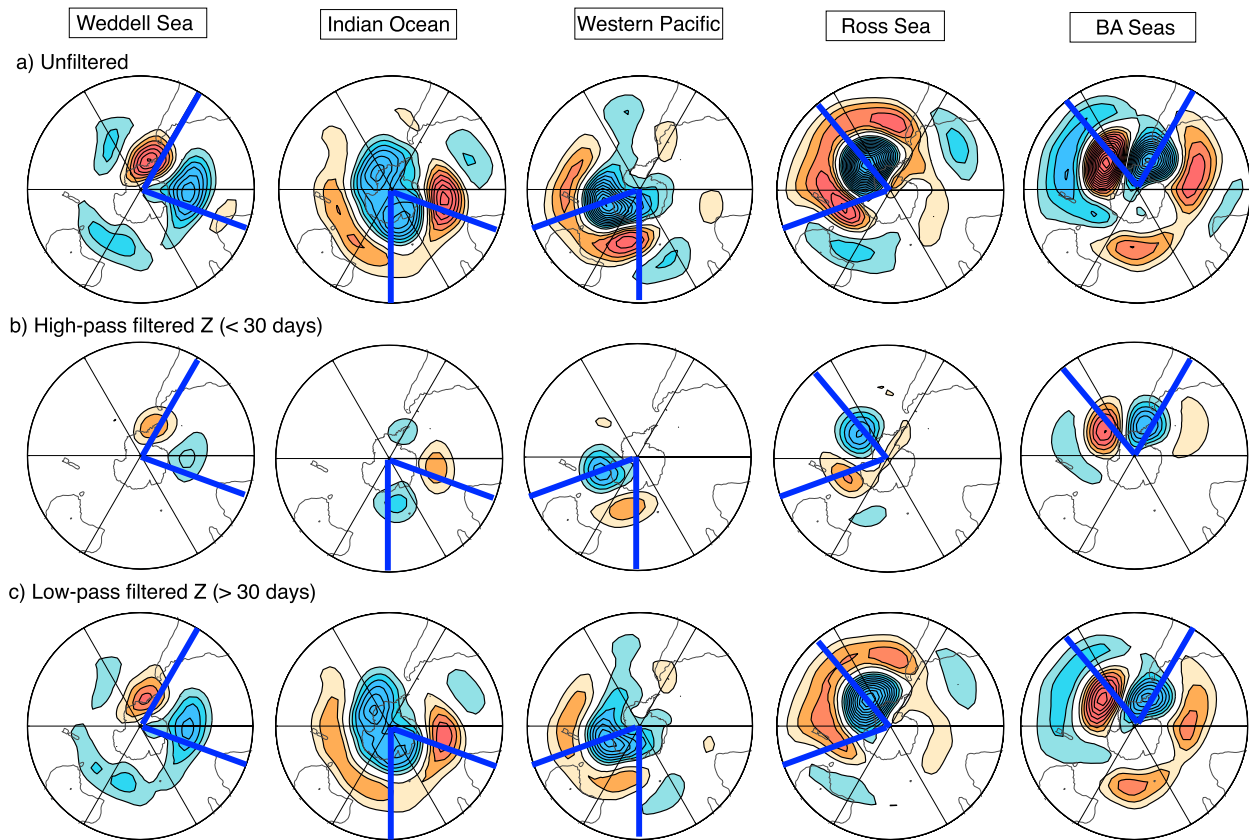


FIG. 3. As in Fig. 2, but regressed onto standardized SIE anomalies for each sector. SIE lags 500-hPa Z by 4 days. Contour interval 3 m. Geographical boundaries of each sector are indicated using blue lines.

et al. 2011) produced by the European Centre for Medium-Range Weather Forecasts (ECMWF), available online at <http://apps.ecmwf.int/datasets/>. We have used 4.5° resolution in both zonal and meridional directions. Geopotential height is calculated by dividing geopotential by standard gravity. The Madden-Julian oscillation (MJO) indices are from Adames and Wallace (2014), who used the first and second EOFs of the difference between the velocity potential fields at 850 and 150 hPa calculated using the ERA-Interim wind fields.

The daily sea ice concentration (S) data are from the National Oceanic and Atmospheric Administration (NOAA)/National Snow and Ice Data Center (NSIDC) Climate Data Record of Passive Microwave Sea Ice Concentration, version 2 (Peng et al. 2013), available online at <http://nsidc.org/data/g02202>. We have used 75-km resolution in both longitude and latitude. The variable used in this study is the merged version of sea ice concentration data created by the Goddard NASA Team algorithm and the Goddard bootstrap. For more information, see Meier et al. (2013). The daily sea ice concentration change (dS/dt) was calculated by subtracting S of the $(n - 1)$ th day of the record from those of

the n th day at each grid box, where n is an integer to designate a particular day.

b. Data processing

Daily climatology is calculated as an average over the years for each calendar day in a year. Then, this seasonal cycle is removed from all the daily data by subtracting the daily climatology from the original data. For monthly data, the same operations are performed but for each month. The linear trend is also removed, except when the trend is discussed.

For the analysis of the intraseasonal time scale using daily data, the outcomes are almost identical whether ENSO is removed or not. This is simply because the ENSO signal has little power in this time scale. For monthly data (except for the ENSO-related analysis), we remove the ENSO signal by linear regression as we shall describe later. When necessary, we analyze the data by binning it into four different seasons: May–July (MJ; ice growing), August–October (ASO; ice maximum), November–January (NDJ; ice melting), and February–April (FMA; ice minimum) as shown in Fig. 1a.

c. Analysis methods

1) CROSS-SPECTRAL ANALYSIS

(i) Formulas

Cross-spectral analysis allows one to reveal linear relationships between two demeaned and detrended time series, $A(t)$ and $B(t)$, by decomposing covariance between $A(t)$ and $B(t)$ into different frequencies. Specifically, we first define a cross-spectral function, $P_{AB}(\omega)$, which is the Fourier transform of cross-covariance function $R_{AB}(m)$ between two time series:

$$P_{AB}(\omega) \equiv \sum_{m=-\infty}^{\infty} R_{AB}(m) \exp(-i\omega m), \quad (1)$$

where ω is angular frequency and m is time lag. Here, $R_{AB}(m)$ is defined as

$$R_{AB}(m) \equiv \overline{A(t+m)B(t)}, \quad (2)$$

in which the overbar denotes a temporal mean. Note that P_{AA} and P_{BB} are the power spectra of $A(t)$ and $B(t)$, respectively.

The real part of $P_{AB}(\omega)$ is called the cospectrum,

$$\text{CO}_{AB}(\omega) \equiv \text{Re}[P_{AB}(\omega)], \quad (3)$$

and the imaginary part of $P_{AB}(\omega)$ is called the quadrature spectrum,

$$Q_{AB}(\omega) \equiv \text{Im}[P_{AB}(\omega)]. \quad (4)$$

The cospectrum can be interpreted as the simultaneous covariance between $A(t)$ and $B(t)$ at each frequency ω , and the quadrature spectrum is the covariance between $A(t)$ and $B(t)$ lagged by $\pi/2$ at each frequency ω . We can also define the phase spectrum:

$$\Phi_{AB}(\omega) \equiv \arctan \left[\frac{Q_{AB}(\omega)}{\text{CO}_{AB}(\omega)} \right], \quad (5)$$

which gives the phase lag between $A(t)$ and $B(t)$ at each frequency ω . Using $\Phi(\omega)$, we can rewrite $P_{AB}(\omega)$ in polar form:

$$P_{AB}(\omega) = |P_{AB}(\omega)| \exp[i\Phi_{AB}(\omega)]. \quad (6)$$

The combinations of these spectral sets [$\text{CO}_{AB}(\omega)$ and $Q_{AB}(\omega)$, or $|P_{AB}(\omega)|$ and $\Phi_{AB}(\omega)$] define any lagged linear relationship between $A(t)$ and $B(t)$.

Last, we define coherence squared, using the above spectra:

$$\text{Coh}^2(\omega) \equiv \frac{|P_{AB}(\omega)|^2}{P_{AA}(\omega)P_{BB}(\omega)} = \frac{\text{CO}_{AB}^2(\omega) + Q_{AB}^2(\omega)}{P_{AA}(\omega)P_{BB}(\omega)}. \quad (7)$$

If we compare this definition with the definition of correlation squared (simultaneous),

$$r^2 \equiv \frac{[\overline{A(t)B(t)}]^2}{\overline{A(t)^2}\overline{B(t)^2}}, \quad (8)$$

which can be viewed as the fraction of variance of $A(t)$ explained by simultaneous $B(t)$, we can regard $\text{Coh}^2(\omega)$ as being a fraction of variance of $A(t)$ explained by $B(t)$, decomposed into each frequency ω , but also including any out-of-phase lagged correlation between them described by the quadrature spectrum. The relationship between the correlation squared and the cospectrum can be written as

$$r^2 = \frac{\sum_{\omega=0}^{\infty} \text{CO}_{AB}^2(\omega)}{\sum_{\omega=0}^{\infty} P_{AA}(\omega) \sum_{\omega=0}^{\infty} P_{BB}(\omega)}. \quad (9)$$

(ii) Application to the data

As described in the data subsection, we use the data from 1979 through 2012 with 2-day time resolution. This means we have time series with length of 12 418 days, and 6209 time steps. When we perform cross-spectral analysis, we first divide the time series equally into $8 + 7 = 15$ overlapped segments (overlap 50%) consisting of $6209/8 = 776$ time steps. Then, we zero-pad the segments into length of $2^{10} = 1024$ time steps by adding 124 zeros to the start and end of each of the 776-member time series sections to make the fast Fourier transform (FFT) process most efficient. Next, we apply a Hamming window with the same length as the zero-padded segments (i.e., 1024 time steps) as a weighting function. This process minimizes artificial effects due to the use of finite data records.

Then, we calculate the power spectra, cospectra, and quadrature spectra for each segment, and average over all the 15 segments. Last, when we calculate $\text{Coh}^2(\omega)$ and phase spectra, we further average the power spectra, cospectra, and quadrature spectra over 64 adjacent frequencies to smooth out the resulting spectra and to increase the degrees of freedom. For example, the sets of 64 frequencies for averaging are chosen as follows: the lowest set is taken from the lowest through the 64th lowest frequency, the second lowest set are taken from the 65th through the 128th lowest, and so on. If we use smaller number of frequency for averaging, we obtain qualitatively the same results, but the spectra become noisier. On the other hand, if we average over larger number of frequencies, the frequency resolution of each spectrum becomes too coarse to see the detailed structure. When drawing spatial maps, we have averaged

over 128 adjacent frequencies (i.e., >32.0, 16.0–32.0, 10.7–16.0, and 8.0–10.7 days in period) for simplicity. This averaging does not affect our qualitative results.

2) MONTE CARLO ESTIMATION

The basic idea of this paper is to estimate the relative importance of climate modes for sea ice by calculating squared-correlation coefficients between various climate indices and SIE time series so that we can compare the SIE variance explained by each orthogonal climate mode. The results of this analysis may depend on the particular period of record, which is relatively short. Therefore, to estimate the true correlation coefficients and their uncertainty more rigorously, we perform the following Monte Carlo procedure when appropriate:

- (i) Choose 17 years out of 34 years (1979–2012) randomly. For reference, the number of possible combinations is about 2.3×10^9 .
- (ii) Calculate correlation coefficients using the randomly chosen 17-yr subset of the data.
- (iii) Repeat steps (i) and (ii) for 1000 times.
- (iv) Calculate the 5th percentile, mean, and 95th percentile of the obtained 1000 correlation coefficients.

3) STATISTICAL DEGREES OF FREEDOM

We use a formula given by Bretherton et al. (1999) to calculate the temporal degrees of freedom N^* to use in statistical tests for the regression/correlation and EOF/principal component (PC) analysis:

$$N^* = N \frac{1 - r_1 r_2}{1 + r_1 r_2}, \quad (10)$$

where N is the original sample size, and r_1 and r_2 are lag-1 autocorrelations of the two time series. Note that $r_1 = r_2$ for calculating the variance (i.e., for EOF/PC analysis), and $r_1 = 1$ for calculating the temporal trend.

4) UNCERTAINTY IN TRUE TRENDS

When discussing the linear trend c of a variable y , (i.e., $y \sim ct + d$, where \sim denotes least squares best fit), we estimate the uncertainty in the true trend slope c using a sample trend \hat{c} and its standard deviation approximated as follows (e.g., Sveshnikov 1968):

$$\hat{\sigma}_c = \frac{\hat{\sigma}_e}{\sqrt{N^*} \sigma_t}. \quad (11)$$

Here, $\hat{\sigma}_e$ is the unbiased standard deviation of the residuals unexplained by least squares best fit, and σ_t is the standard deviation of the sampling time. Then, the variable

$$C = \frac{\hat{c} - c}{\hat{\sigma}_c} \quad (12)$$

is distributed like a t statistic with $N^* - 2$ degrees of freedom. Hence, we can put limits on the true slope c :

$$\hat{c} - t_{\alpha}^{N^*-2} \hat{\sigma}_c < c < \hat{c} + t_{\alpha}^{N^*-2} \hat{\sigma}_c, \quad (13)$$

where $t_{\alpha}^{N^*-2}$ is the critical value of the t statistic for confidence level α and degrees of freedom $N^* - 2$.

3. Coherent frequency bands between geopotential height and sea ice extent

Our first goal is to find the time scale for which the atmosphere explains the largest fraction of sea ice variance. To achieve this, we use cross-spectral analysis. In this particular analysis, we use Z at 500 hPa to represent meteorology and SIE for sea ice, and perform cross-spectral analysis between Z at each grid point and SIE at each sector.

The power spectra for Z and SIE are denoted as $\overline{P_Z}(\omega; \lambda, \phi)$ and $\overline{P_{SIE}}(\omega; i)$, respectively, where ω is angular frequency, λ is longitude, ϕ is latitude, i is an index to denote sectors ($i = \text{WS, IO, WP, RS, or BA}$), and the overbars denote the average over different realizations (see the method section). Both of the power spectra exhibit typical features of red noise without any statistically significant periodicity that would reject a null hypothesis that the time series are red noise at 95% confidence (not shown). Next, we have calculated coherence squared [$\text{Coh}^2(\omega; \lambda, \phi; i)$] at each grid as follows:

$$\text{Coh}^2(\omega; \lambda, \phi; i) = \frac{\overline{\text{CO}_{Z,SIE}}(\omega; \lambda, \phi; i)^2 + \overline{Q_{Z,SIE}}(\omega; \lambda, \phi; i)^2}{\overline{P_Z}(\omega; \lambda, \phi) \overline{P_{SIE}}(\omega; i)}, \quad (14)$$

where CO is the cospectrum and Q is the quadrature spectrum. As described in the method section, Coh^2 serves as the squared-correlation coefficient decomposed into different Fourier modes, giving the fraction of the variance of SIE explained by Z in percent at each frequency.

Figure 4a shows the Coh^2 maps for four different frequency bands calculated for SIE of each sector. We note that the degrees of freedom are the same for all four frequency bands so that the statistical significance of Coh^2 also remains fixed. For all sectors, the maximum Coh^2 is associated with a similar spatial pattern in the Z field across all time scales. The magnitude of Coh^2 fluctuates substantially depending on the time scale, however.

We then look at the Coh^2 spectra at the grid point where Z shows maximum coherence with the SIE time

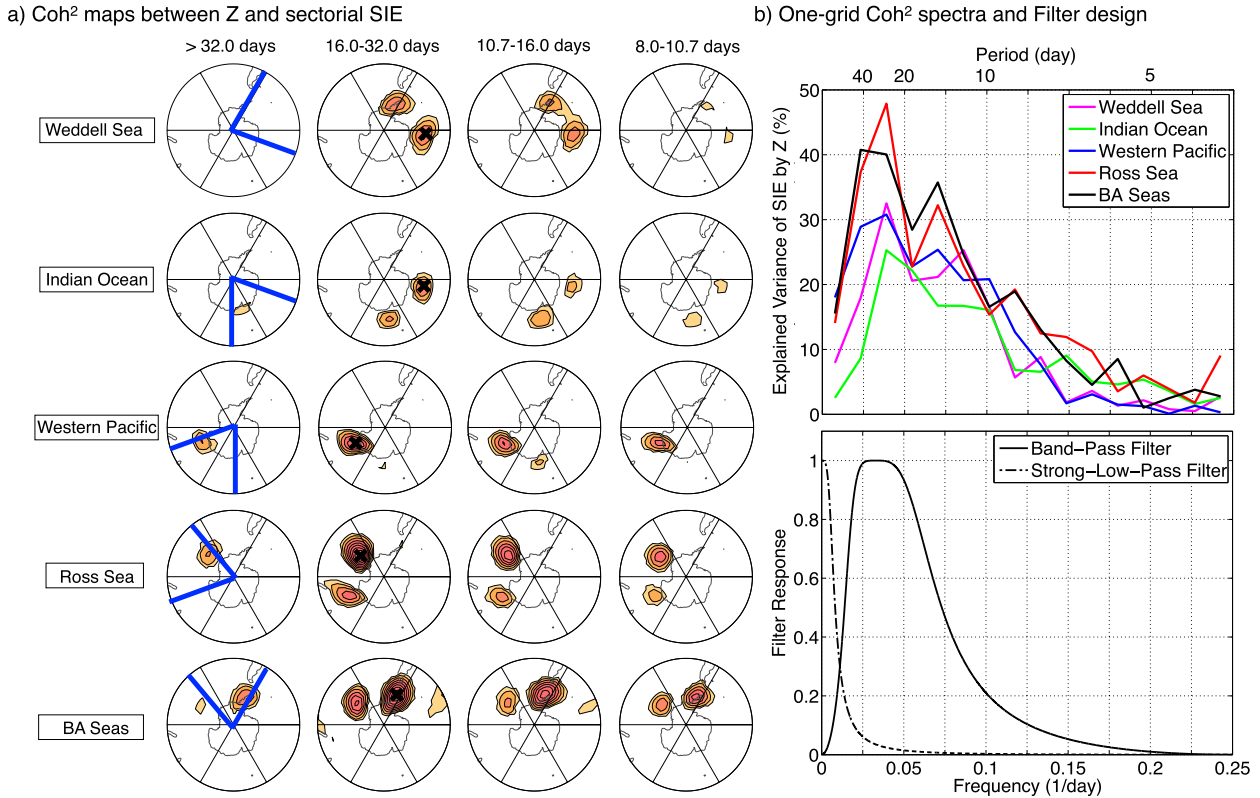


FIG. 4. (a) Coh^2 maps between Z at 500 hPa and SIE time series for each sector (rows) and for each frequency band (columns). Contour interval is 5%, but drawn for 10% and larger. Blue lines indicate geographical boundaries of each sector, and crosses in the second column indicate the most coherent grids for each sector. (b) Coh^2 spectra between Z at the 500 hPa and SIE time series at the most coherent grids shown in (a). (c) Filter responses for two different filters.

series of each sector (shown as black crosses in the second column of Fig. 4a). The representative grid points used in this analysis are (60°S , 10°E) for the WS and IO sector, (60°S , 150°E) for the WP sector, (60°S , 130°W) for the RS sector, and (60°S , 60°W) for the BA sector. The upper panel of Fig. 4b shows that the Coh^2 reaches its maximum for frequencies around $0.02\text{--}0.05 \text{ day}^{-1}$, or in the period range, $\sim 20\text{--}40$ days, for all the longitudinal sectors. For reference, 95% significance level for coherency with 125 degrees of freedom is 2.4% (Amos and Koopmans 1963): this means, at virtually all frequencies shown here, the coherence is significant at 95%. Across this range of periods, the phase lag between Z and SIE remains relatively stable at about $40^\circ\text{--}70^\circ$ (not shown).

From this analysis, we can conclude that Z and SIE are most coherent at periods between about 20 and 40 days in Southern Hemisphere. One might wonder how to reconcile this result with Fig. 3, which clearly shows that variability on time scales >30 days have a larger projection onto unfiltered Z than those on time scales <30 days. It is important, however, to remember that coherence is a measure of covariance normalized

by a product of variance, just like correlation, but decomposed into each frequency. Therefore, large coherence between Z and SIE means that a large fraction of SIE variance is explained by Z at a particular frequency but there is not information about the actual amount of variance, or amplitude, explained at the frequency. Because both Z and SIE are typical red noise time series, the actual amount of SIE variance explained by Z is larger for interannual time scale: that is why >30 -day variability has a larger projection in Fig. 3.

4. Intraseasonal time scale

In this section, we focus on the intraseasonal time scale (20–40 days) for which Z and SIE are most coherent. Although the contribution of this time scale to the total SIE variance is small, it is important to learn the dynamics of the covariability between sea ice and Z by investigating the time scale for which atmosphere and sea ice are most tightly coupled. Then we estimate the relative importance of various forms of atmospheric variability for Antarctic sea ice. The estimation

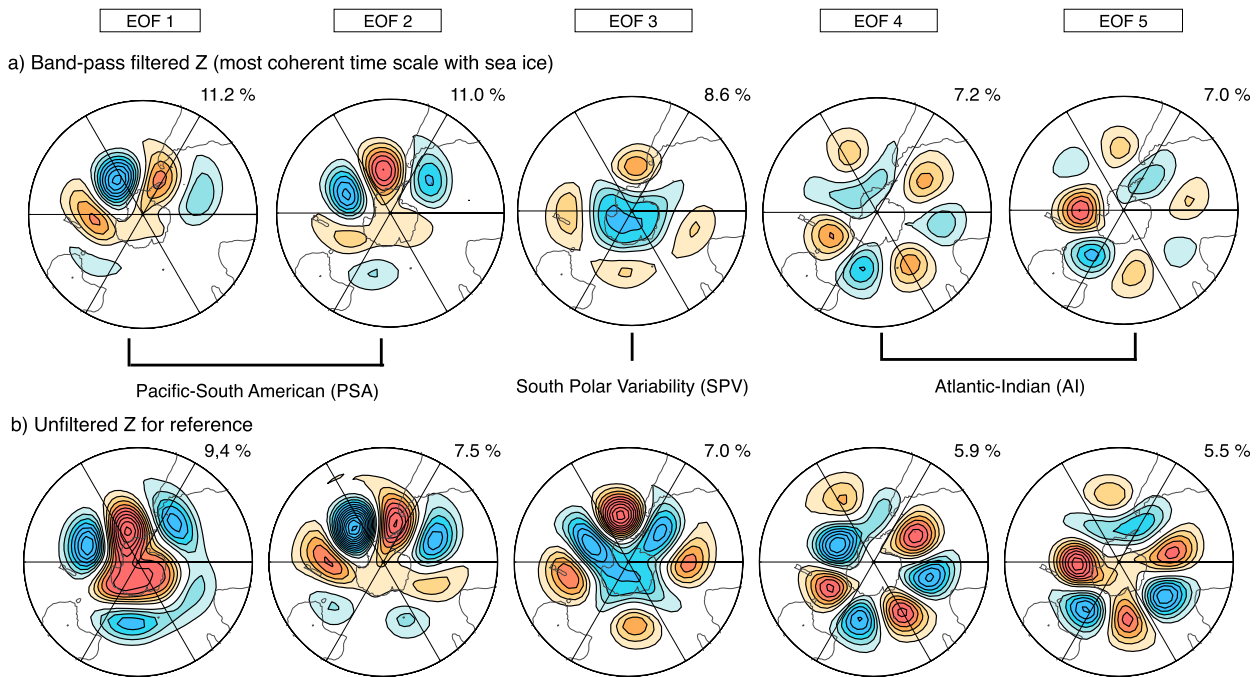


FIG. 5. (a) As in Fig. 2, but for bandpass filtered Z at 500 hPa for the time scale where Z is most coherent with SIE. (b) As in (a), but for unfiltered Z at 500 hPa. The first three EOFs are identical with Fig. 2a.

is based on several uncorrelated climatological indices obtained from the following procedure.

a. EOF/PC analysis for the hemispheric domain

First, to exploit the signal in the most coherent frequency band, we construct a bandpass filter shown in the lower panel of Fig. 4b, and apply it to Z at 500 hPa. Then, to find the most dominant intraseasonal meteorological modes of variability, we perform EOF/PC analysis to calculate the EOFs of Z south of 30°S. The first five EOFs are statistically well separated from the rest of the EOFs by the criterion of North et al. (1982). The EOFs give us a general idea about the “preferred” spatial patterns in the atmosphere. PC time series serve as climate indices associated with each EOF spatial pattern. PC1 explains the largest variance in the Z data, and each following PC is not correlated with any other. We hereafter call each of EOF n spatial patterns (shown in the form of regression maps onto PC n) and its corresponding PC n time series the “ n th EOF mode.”

The first and second EOF modes in Fig. 5a are not well separated from each other by the North et al. (1982) criterion, and it is found that PC2 leads PC1 by 4–6 days by lag correlation analysis (not shown). The spatial and temporal patterns of these two modes are in quadrature. These two modes together form a wave train that propagates eastward following the background flow. In the meteorological community, these waves are well

known and are called quasi-stationary Rossby waves (e.g., Hoskins et al. 1977; Hoskins and Karoly 1981). They are excited by many sources, such as orography, heat sources, instabilities, and other waves or eddies (e.g., Holton and Hakim 2012). The pattern explained by EOF1 and EOF2 is similar to what is often referred to as the Pacific–South American (PSA) pattern (e.g., Mo and Higgins 1998), which is known to arise naturally in this region through atmospheric dynamics as well as in response to heating. We also use this nomenclature in this particular study, because our EOF1 and EOF2 presumably have many common features with PSA. We note, however, that our PSA mode is derived only for intraseasonal time scales, so it may also have different features from the “canonical” PSA.

From a more local perspective, the PSA mode could be viewed as the bandpass-filtered Amundsen Sea low (ASL) variability (e.g., Turner et al. 2013). To check the variability directly associated with ASL, Hosking et al. (2013) defined an index called the “ASL relative central pressure” index. They showed, however, that the index cannot capture the sea ice modulation very well, mainly because the index has only amplitude information and does not give any information about the position of the low. In this sense, our definition of PSA index (i.e., PC1 and PC2) is an improved version of ASL relative central pressure index, because we can capture information about both amplitude and position of the low.

The third EOF mode in Fig. 5a shows a relatively zonally symmetric pattern that oscillates coherently around the South Pole. This mode, which we refer to as south polar variability (SPV), is significantly correlated at 95% confidence with bandpass-filtered SAM index, and it explains about 25% of the variance of the filtered SAM index. The fourth and fifth EOF modes again compose a Rossby mode, whose lag correlation relationship is almost the same as the PSA. This mode exhibits Rossby wave signals in the Atlantic and Indian Ocean sectors, so we call this Rossby mode the Atlantic–Indian (AI) pattern. Kidson (1999) considered a similar pattern in the intraseasonal (10–50 day) 300-hPa streamfunction variability.

We note that the above modes (Fig. 5a), especially the Rossby wave patterns, also emerge from PC analysis of unfiltered Z anomalies in noisier forms (Fig. 5b). This confirms that the structures shown in EOFs of bandpass filtered data are based on solely atmospheric variability, and that the patterns do not owe their existence to statistical covariability with sea ice.

One of the main ideas of this paper is that these Rossby modes deserve more attention in the context of understanding sea ice variability, particularly since Rossby waves are one of the most dominant atmospheric modes of variability. It is also worth pointing out that, even though the Rossby modes shares some variance with SAM, the spatial structures of the Rossby modes are not similar to SAM. This means that, at least for the intraseasonal time scale, it is essential to look at Rossby wave structures, rather than looking only at the SAM itself, which has received much attention for explaining sea ice modulation. We also note that these Rossby modes are not related to ENSO, simply because ENSO does not have much power in this time scale. Removing the influence of the MJO from Z data by linear regression yields no major changes in the present results. This is because the teleconnection signal of the MJO is too small in the Southern Ocean, compared to those of other climate modes.

b. EOF/PC analysis for the local domain

Because EOF/PC analysis seeks spatial patterns that explain the largest variance in a prescribed domain, local weather disturbances are not well captured by EOFs of the hemispheric domain as computed in the previous subsection. Therefore, we further perform EOF/PC analysis for local longitudinal sectors shown in Fig. 1 after removing the hemispheric EOF modes by regression. This procedure gives us indices for localized weather modes that are not correlated with each other or with the hemispheric modes. We can check whether local meteorology shares some variance with SIE using

these modes, but each mode should not be interpreted as having any unique physical identity.

c. Relative importance of the different climate modes for sea ice variability

We have prepared various climate indices that are not correlated with each other. In this subsection, we calculate r^2 between these climate indices and SIE time series [r^2 can be viewed as the fraction of variance of SIE explained by a climate index; see Eqs. (8) and (9)] and compare the magnitude among the climate modes. We can also sum the r^2 of the climate modes and find the total variance explained by them, because these climate indices are uncorrelated. If a mode consists of two indices (e.g., PSA mode consists of PC1 and PC2), we can simply add the fraction of variance to find the explained variance by the mode. For example, if correlations between SIE and PC1 (PC2) are 0.5 (0.8), the explained variance by PC1 and 2 is $0.5^2 + 0.8^2 = 0.89 = 89\%$. The sum never surpasses 100% as long as PC1 and PC2 are temporally uncorrelated.

When calculating r^2 , we use a lag of 4 days (meteorology leads sea ice), because spectral analysis shows that meteorology leading by about 4 days explains the largest total variance of sea ice for this time scale. The results do not change much if we use slightly different lags, however. We shall further investigate this issue using lag regression analysis in the next subsection.

A caveat for this analysis is that we use the spatial pattern derived from all the month to explain the seasonal SIE variability. This is mainly because the EOF/PC modes for seasonal data are not distinct according to the North et al. (1982) criteria, presumably due to the more limited sample size. Therefore, here we use the EOF/PC patterns derived from all 12 months, which works reasonably well. For reference, Fig. S1 (see the supplemental material) compares the seasonal PSA modes with the all-month PSA shown in Fig. 5a. The seasonal patterns are noisier, but they are qualitatively not too different from the structures obtained using all the months, since the seasonal cycle in extratropical winds and temperature is relatively weak in the Southern Hemisphere.

Figure 6 shows r^2 between the sectorial SIE and the various climate modes for each season. These results support the notion that a large portion of the intraseasonal variability can be explained by Rossby modes, especially in the MJJ and ASO seasons. It is also notable that about 45% of the intraseasonal sea ice variability in the BA and RS sectors can be explained by the PSA mode. On the other hand, a large fraction of SIE variability in the IO sector is associated with more local weather. We note that ENSO does not have an intraseasonal component in its variance spectrum.

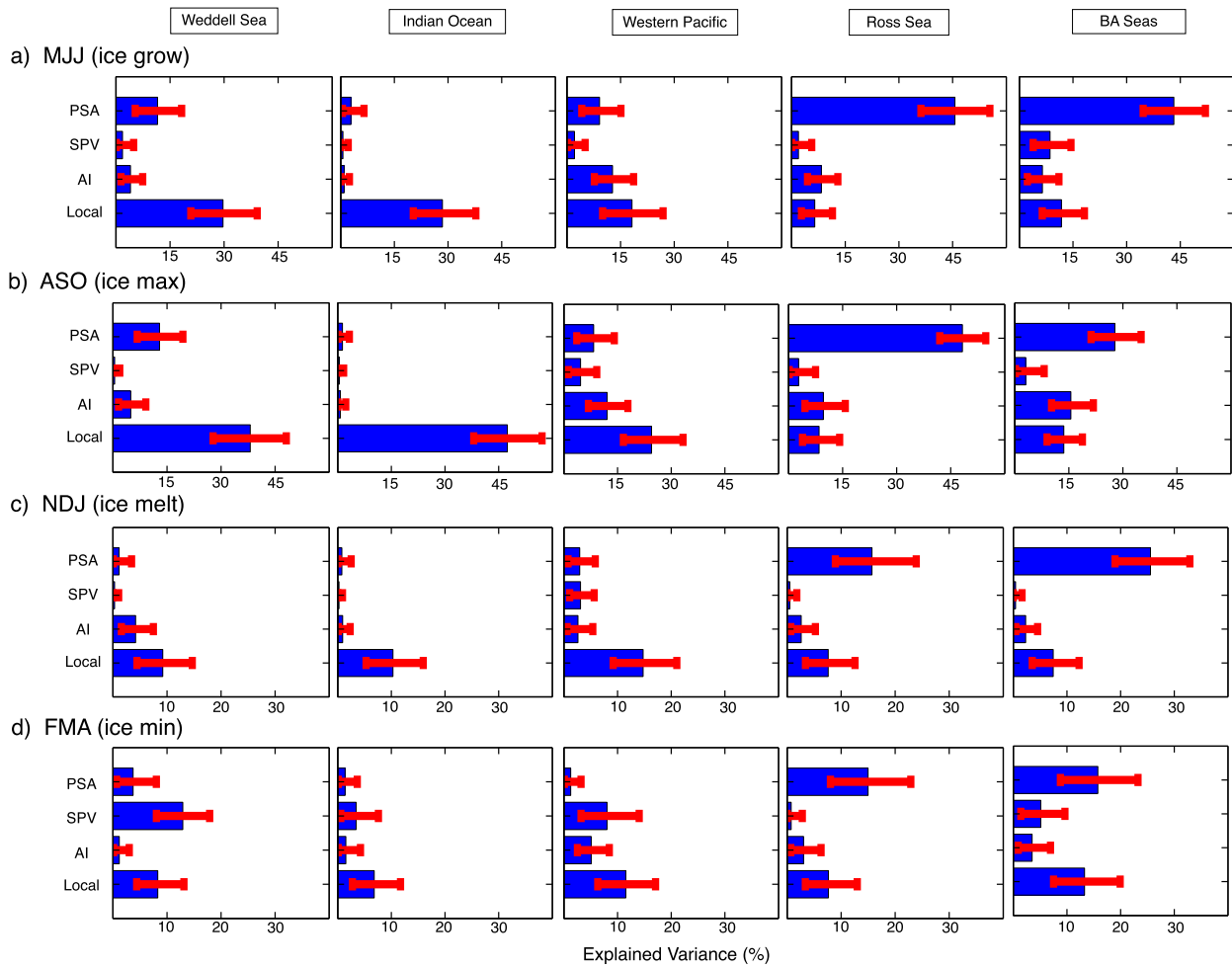


FIG. 6. Explained variance (%) of SIE time series in five longitudinal sectors by various intraseasonal (bandpass filtered) climate modes shown in Fig. 5a. SIE lags Z by 4 days. Each climate index is not correlated with each other. Blue bars show the mean of 1000 squared-correlation coefficients calculated for randomly chosen 17 years out of 34 years, repeated 1000 times (see method section). Red error bars show the 5th and 95th percentile value of the 1000 coefficients. Local variability is defined as the first five EOFs of the local domains (see section 4b).

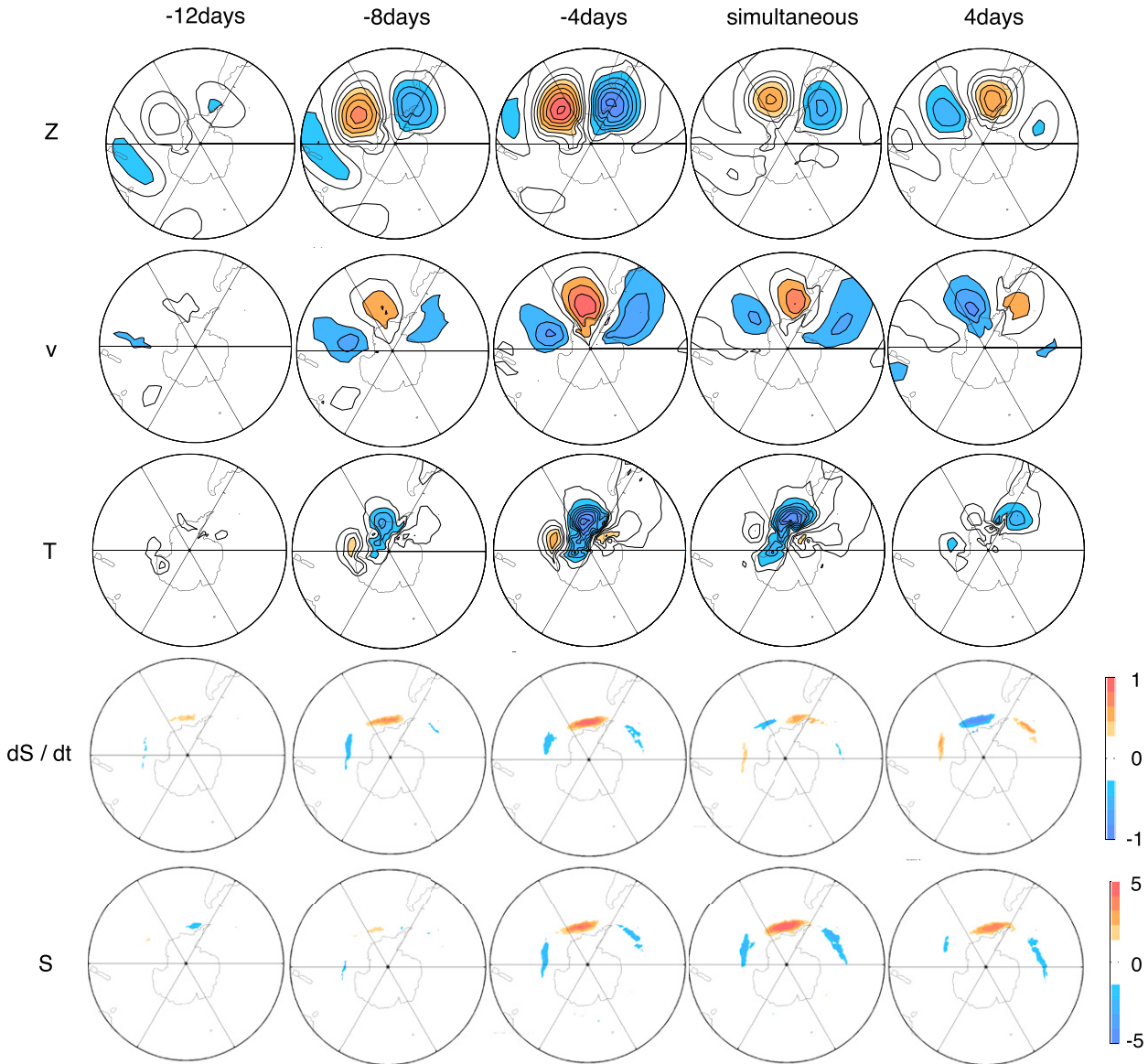
The total explained variances in NDJ and FMA are about a half or less of those in MJJ and ASO. This result suggests that it is more difficult to predict intraseasonal sea ice variability by meteorological variables during austral summer. This might be due to the fact that the variance of sea ice is smaller in austral summer because there is much less sea ice, and therefore the signal-to-noise ratio becomes smaller. It is also possible, however, that the annual mean meteorological patterns better represent the MJJ and ASO seasons.

d. The mechanism of how Rossby waves modulate sea ice

To confirm that Rossby waves play a dominant part in modulating SIE, and to clarify the mechanism of how Rossby waves modulate Antarctic sea ice, we perform

lag regression analysis of five variables (daily Z , v , and T at 1000 hPa, and dS/dt and S ; bandpass filtered) onto standardized SIE. Figure 7 shows the lag regression maps of the five variables on the reference SIE time series of BA sector. The patterns in Z and v show a robust geostrophic relationship, suggesting typical features of Rossby waves whose phase propagates eastward. The v pattern corresponds to the T and dS/dt patterns in the way expected to produce positive anomalies in S .

Southerly anomalies presumably yield cold advection, so that sea ice grows, and vice versa. These dynamical and thermodynamical effects of meridional wind in the Southern Ocean are already well investigated for many different time scales (e.g., Lefebvre and Goosse 2005; Renwick et al. 2012; Holland and Kwok 2012). The anomalous meteorological signal is largest when SIE



Downloaded from http://journals.ametsoc.org/jcl/article-pdf/29/2/721/4067739/jcl-d-15-0301_1.pdf by UNIVERSITY OF AUCKLAND user on 30 June 2020

FIG. 7. Lag regression maps of daily Z , v , T , dS/dt , and S (Z , v , and T are at the 1000-hPa level) on the standardized daily SIE time series of BA sector. The numbers of days of lags are indicated above the maps, where positive (negative) number indicates SIE leads (lags) the other variables. Contour intervals 5 m for Z , 0.4 m s^{-1} for v , and 0.25 K for T . Zero contours are omitted. Positive (negative) local maxima are shaded orange (blue).

lags meteorology by 4 days, as documented by Renwick et al. (2012).

One might be confused about how to reconcile the lag of 4 days and the period of 20–40 days. As we mentioned in the previous section, the phase difference between meteorology and SIE stays constant about 40° – 70° across the intraseasonal time scale. If the phase lag between meteorology and SIE is 60° , then the time lag is $60/360^\circ$ of one period (i.e., meteorology generally leads sea ice by one-sixth of the period). Therefore, the lag of 60° yields the lag of

4 days between meteorology and SIE if we look at the Fourier mode of 24 days in period. It is thus consistent that the lag between meteorology and sea ice is about four days, with its uncertainty depending on which Fourier period in 20–40 days is most coherent at each longitude.

5. Interannual time scale

In this section, we perform the same analysis as the previous section but for unfiltered monthly mean

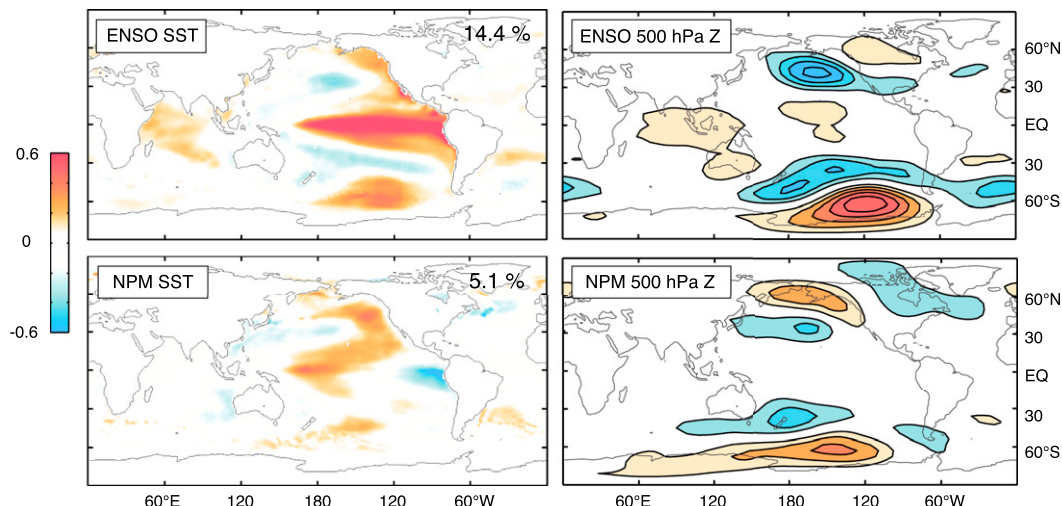


FIG. 8. (left) Regression maps of monthly global sea surface temperature (SST; $^{\circ}$ C) onto its standardized PC1 (ENSO) and PC2 (NPM) time series for all months. Monthly climatology and the linear trend are removed beforehand. Variance contributions are indicated on top right. (right) Regression maps of Z at 500 hPa onto the PC1 (ENSO) and PC2 (NPM). Contour interval is 5 m. Zero contours are omitted, and positive (negative) local maxima are shaded orange (blue).

anomalies, which represent interannual time scales. Even though Z and SIE are less coherent, this time scale is important because the magnitude of sea ice variance (i.e., not the fraction of variance) explained by Z is still much larger than that of the intraseasonal time scale. This is due to the long persistence of sea ice anomalies.

We have removed the atmospheric variations that are related to tropical SST by regressing out two modes of variability associated with the ENSO patterns in Fig. 8, except in those cases where we specifically investigate the influence of ENSO. The ENSO modes are obtained as the first two modes from EOF/PC analysis performed on the global SST. The first mode is well-known ENSO, and the second mode is called the North Pacific mode (NPM) (Hartmann 2015). This mode shares about a half of its total variance with so-called ENSO Modoki (Ashok et al. 2007) or central Pacific (CP) ENSO (Kao and Yu 2009). The teleconnection patterns for these modes are shown in Fig. 8, right, (global view) and Fig. 9a (polar view).

Figure 9b shows the first three EOFs of unfiltered monthly Z after removing the ENSO signal. For this time scale, the first mode captures SAM, and the second and third modes capture the Rossby wave-like structure prevalent across the Drake Passage (DPR). For this time scale, PC2 and PC3 do not show any lag correlations, meaning that monthly data do not resolve the propagation of the waves, but rather more stationary anomalies. One possible ultimate cause for this mode could still be signals coming from the Pacific, which may remain even after removing the two leading EOF modes of tropical SST by simultaneous linear regression. This

mode could also be generated through interaction among eddies, jets, and topography in the extratropics.

The analysis of relative importance for sea ice variability (Fig. 10) shows somewhat different features from the intraseasonal time scale. We did not employ any lags for the interannual time scale, because the simultaneous squared correlations are larger than with any other lag. In each sector, sea ice is modulated by different phenomena. Sea ice in the IO sector is modulated by SAM and ENSO, in the WP sector by local meteorology, in the RS sector by ENSO and DPR, and in the BA sector by DPR. SIE in the WS sector is less well explained by these climate modes. Major features shown here are independent of season, except for the IO sector; SIE in the IO sector is mainly explained by SAM in MJJ, but ENSO becomes of more importance in NDJ and FMA.

The influences from ENSO and SAM appear important for the interannual time scale, but the DPR modes also explain SIE variance comparable to that explained by ENSO and SAM. Investigating the ultimate cause of the DPR modes is beyond the scope of this study, but this result supports the notion that linear analyses of ENSO and SAM are not sufficient to understand interannual sea ice variability.

6. Trends of interannual climate modes and its implications for the sea ice trends during the satellite era

The extent of Antarctic sea ice is known to have expanded during the satellite era (Parkinson and Cavalieri

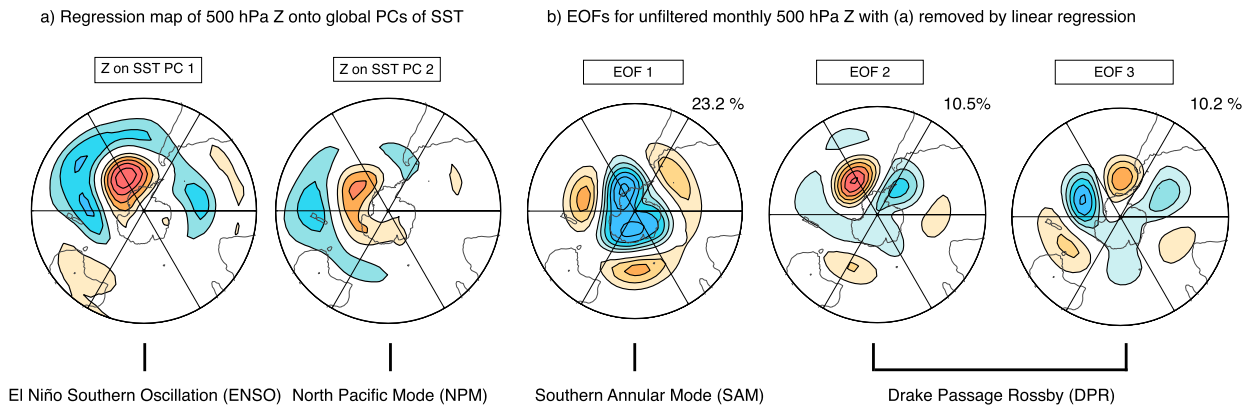


FIG. 9. (a) As in Fig. 8 (right), but for SH polar stereographic projection. (b) As in Fig. 2, but for unfiltered monthly data. The climate modes shown in (a) are removed by linear regression beforehand.

2012). We have much observational and modeling evidence that these trends are driven by atmospheric (e.g., Holland and Kwok 2012) or oceanic (e.g., Zhang 2007) modulation, but the ultimate cause of the atmospheric/oceanic variability that forces sea ice to increase still remains unexplained. Anthropogenic forcings such as ozone depletion have also received much attention as one of the root causes (e.g., Turner et al. 2009), but other studies suggest otherwise (Bitz and Polvani 2012). Polvani and Smith (2013) argued that the observed trend in Antarctic sea ice falls within the natural variability exhibited by phase 5 of the Coupled Model Intercomparison Project (CMIP5) models.

In this section, we investigate the implications of the ENSO, NPM, SAM, and DPR modes for the sea ice trend during the period 1979–2012. Even though these are interannual climate modes, some of them have had a nonnegligible trend during the satellite era. For example, the eastern equatorial Pacific Ocean is known to have a cooling trend during the satellite era (Fig. 11a), and therefore, the trend pattern in Z (Fig. 11b) has a large projection onto our ENSO mode (Fig. 9a). Consequently, our ENSO mode has a negative (i.e., so-called La Niña like) trend during the satellite era (Fig. 11c, top). Observed trends in the Southern Hemispheric atmospheric circulation during the satellite era in late spring and early summer have received much attention in relation to ozone depletion (e.g., Polvani et al. 2011). The associated trend is also evident in Fig. 11b, and therefore, it projects onto our SAM mode (Fig. 9b), yielding a positive SAM trend (Fig. 11c, bottom).

Our main goal in this section is to explore the influence of these climatological trends on Antarctic sea ice trends during the past 34 years. Our analysis below is based on pure statistical analyses for the observational data of the satellite era. We acknowledge that obtaining statistical results is not the ultimate goal of the research

community. Statistical results, however, could potentially serve as strong tools to provide evidence for the underlining physical processes and mechanisms.

a. Method

The idea of our analysis is to use linear regression to isolate the sea ice trends associated with the interannual climate modes. Specifically, the method includes the following steps:

- 1) Obtain a “with trend” climate index, by projecting the nondetrended Z data onto the spatial pattern associated with the interannual climate mode shown in Fig. 9, which have been identified in detrended data.
- 2) Take annual averages of the obtained climate index and SIE time series, which gives two sets of 34 data points of 1979–2012.
- 3) Remove the sea ice modulations associated with the climate index from the SIE time series, by using the regression coefficient calculated between the detrended climate indices and SIE with 34 points each (Fig. 12). When calculating the regression coefficient, the trends of both time series are removed so that only nontrend variability affects the regression coefficients.
- 4) Check whether the “residual SIE time series” still has a significant trend at 95%. The statistical uncertainty of the trend is estimated using the method described in section 2c(4).
- 5) Seasonal analysis: Repeat steps 2 through 4 using data sorted into seasonal bins.

Unlike the previous section, the with-trend indices obtained in step 1 are no longer temporally orthogonal with each other. For instance, the indices between “with-trend ENSO” and “with-trend SAM” share 38% of variance with each other (Fig. 11c). This means the ENSO trend may influence the SAM trend, and vice versa. Therefore, with-trend ENSO should not be viewed

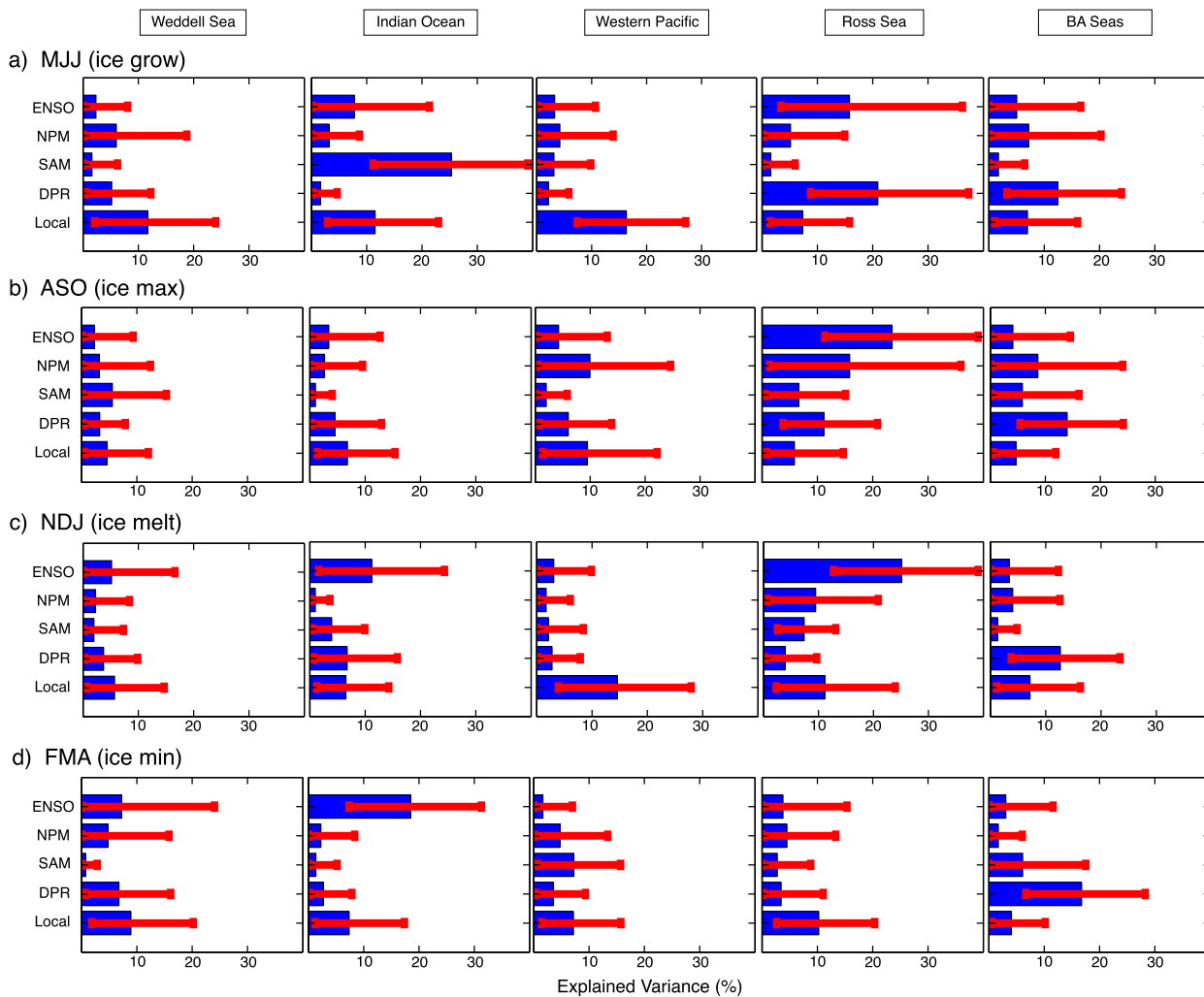


FIG. 10. As in Fig. 6, but for unfiltered monthly data without any lags. Each mode is shown in Fig. 9. Local variability is defined as the first three EOFs of the local domains (see section 4b).

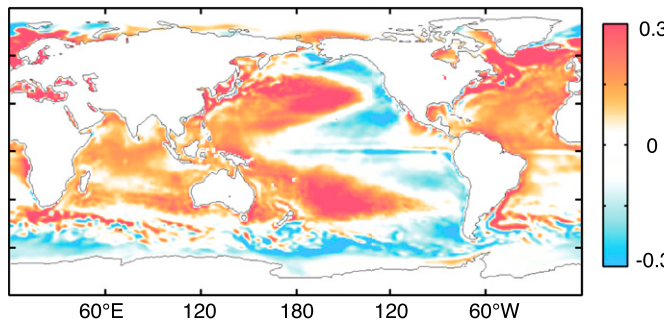
as an independent component from SAM or other climate modes. Rather, each with-trend index represents different perspectives of how to define the climate modes.

Figure 12a shows the scatterplots based on annual mean data showing the linear relationship between sectorial SIE and ENSO used in step 3. As shown in the previous section, SIE variations are best explained by ENSO in the RS sector, with the IO sector being second best. Correlations between ENSO and SIE in the WP and BA sectors are insignificant. The same analysis for SAM is summarized in the Fig. 12b. SAM explains sea ice in the IO sector relatively well, but the other sectors are not well explained by SAM. This is also consistent with the results shown in the previous section. We calculate these regression coefficients using detrended data so that the regression coefficient depends only on the year-to-year variability and not the trend. The robustness

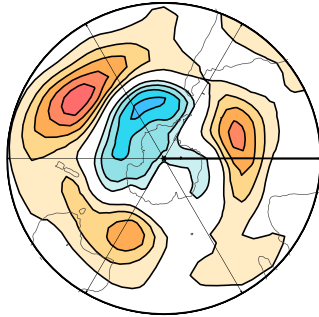
of this regression coefficient is extremely important, because the estimated trend associated with each climate mode is sensitive to this coefficient.

One might suspect we should also investigate the AMO or Pacific decadal oscillation (PDO), which are two dominant decadal modes of variability on Earth. In principle, the answer is yes. In practice, however, it is hard to investigate multidecadal modes with an available record of 34 years because of the lack of enough statistical degrees of freedom. Therefore, the results shown here may be affected by decadal variability, such as the AMO and PDO. Even though it is beyond the scope of this study, it is possible to investigate the decadal variability with a help of model results. Li et al. (2014) proposed a physical explanation of the trend by the AMO. They argued that Atlantic warming generates deep convection, and the resulting stationary Rossby

a) Trend of SST anomalies from 1979 through 2012



b) 500 hPa Z trend from 1979 through 2012



c) With-trend indices

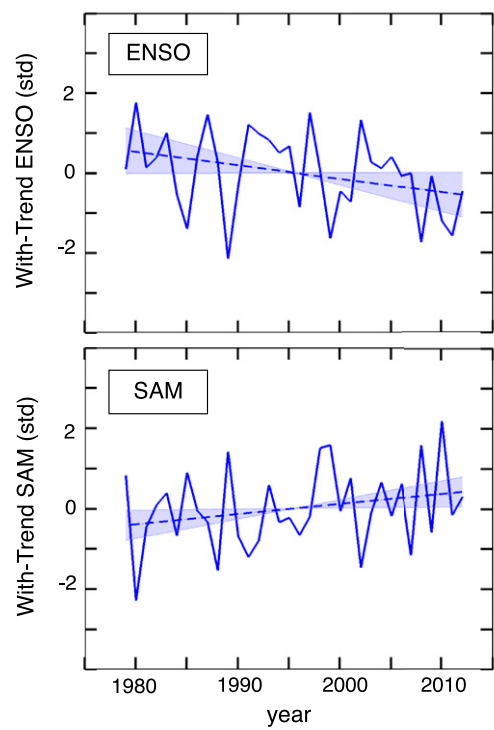


FIG. 11. (a) Linear trends of SST ($^{\circ}\text{C decade}^{-1}$) from 1979 through 2012 calculated at each grid. (b) As in (a), but for Z at 500 hPa. Contour interval 2 m decade^{-1} . Zero contours are omitted, and positive (negative) local maxima are shaded orange (blue). (c) With-trend climate indices calculated by projecting the nondetrended Z data onto the spatial patterns of ENSO and SAM shown in Fig. 9. Dashed lines are calculated by least squares fitting, and shaded areas show the uncertainty of the slopes at the 95% confidence level.

wave trains deepen the Amundsen Sea low, and thus redistributes the sea ice concentration between the RS and BA sectors through thermal advection and mechanical forcing. The teleconnection between Atlantic warming and Southern Hemisphere atmospheric circulation changes are well supported by a hierarchy of climate model simulations (Li et al. 2015a,b; Simpkins et al. 2014), while the interactions between local circulation changes and sea ice concentration changes are investigated by several recent studies (e.g., Holland and Kwok 2012). A caveat of these studies, however, is that the AMO's variance contribution to the Amundsen Sea low and corresponding RS and BA sea ice responses await further observational verification using data with a longer time span than the past three decades.

b. Results

1) ENSO

Figure 13a shows the SIE time series before and after regressing out the sea ice modulation associated with ENSO. In this figure, we highlight the RS sector because we have an a priori expectation that ENSO influences

the sea ice in the RS sector most efficiently (Figs. 10 and 12a). After regressing out ENSO, the slope of the trend during the satellite era is reduced in the RS sector. In fact, after removing the effect of ENSO, the positive trend of SIE for the RS sector is no longer significant at the 95% confidence level. This means that, even though the “sample trend” for this particular time span is still positive, the “true trend” might be zero except for the influence of ENSO. In other words, if we prepare a random time series with the same degrees of freedom and standard deviation as the residual SIE time series, we have a very good chance to obtain a positive trend with the same magnitude purely by chance.

Antarctic sea ice is expanding, which is contrary to what we have observed in the Arctic, and contrary to climate model predictions of the response to global warming. However, if the standard deviation of sea ice time series is large enough, and if the time span is short enough, it is likely that the positive trends could appear by chance. In this sense, it is less puzzling if the positive trend is statistically insignificant, because we have a very good chance (i.e., more than 5%) to obtain the observed magnitude of the trend simply by stochastic variability

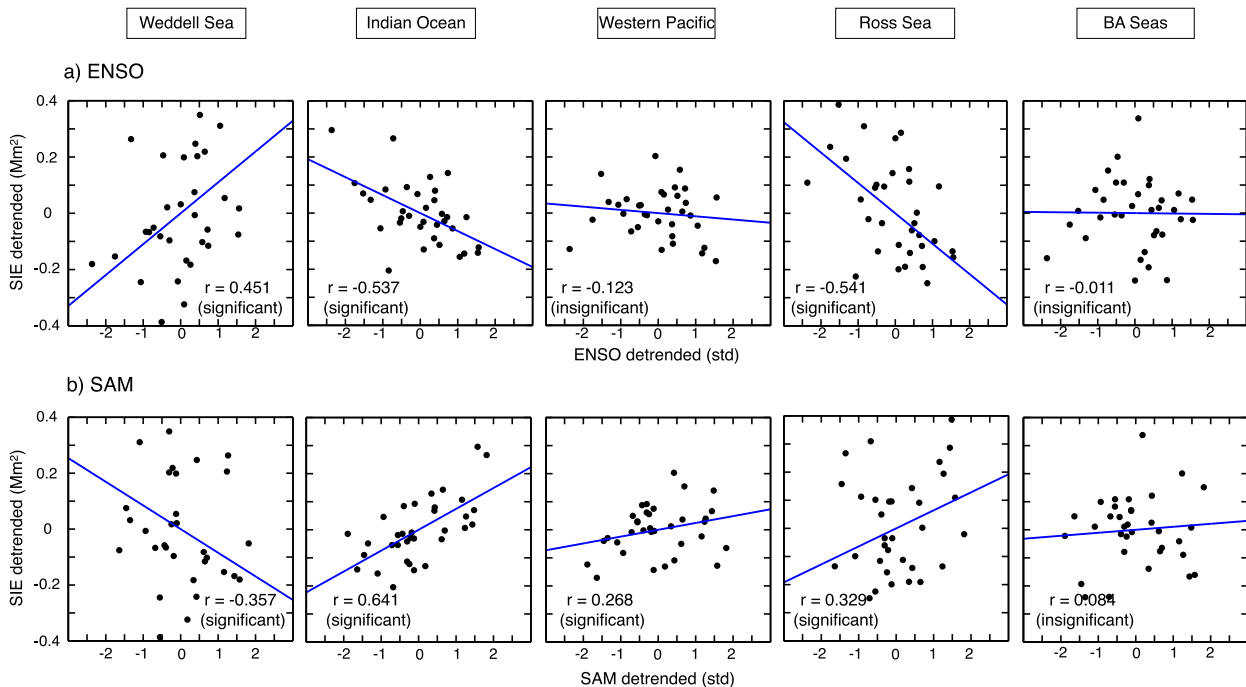


FIG. 12. (a) Scatterplots showing the relationship between SIE time series for each sector and the ENSO index shown in Fig. 11c, but both time series are detrended. Blue lines are calculated by least squares fitting. Correlations r and their significance at the 95% confidence level are shown on bottom in each panel. (b) As in (a), but for SAM.

rather than by some deterministic causes. Here, “stochastic” variability refers to variability that originates from internally generated variability whose statistics are stationary, rather than from a true secular trend. This view is encouraged by the result that the sea ice trend in the past 34 years loses its statistical significance at 95% after removing the influence of one particular climate mode, in this case ENSO.

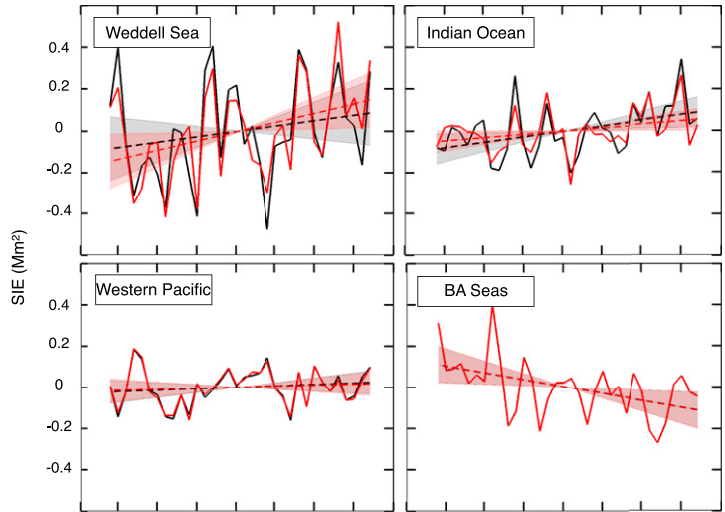
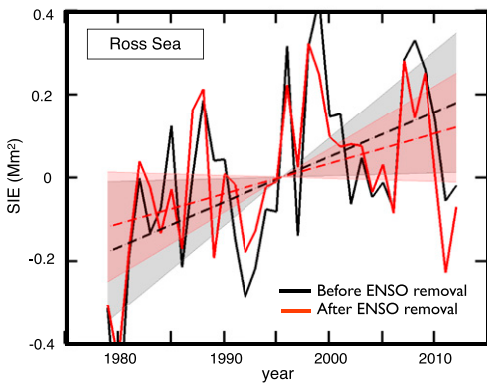
The same conclusion as the RS sector stands for the IO sector, where the increasing trend becomes barely insignificant at the 95% confidence level. Conversely, the sea ice trend in the WS sector becomes significant after regressing out ENSO. This result is also novel, because it means the positive WS trend has partly been masked by ENSO variability. Because of this counteraction among SIE in the RS, IO, and WS sectors, the trend of the hemispheric SIE time series remains significant at 95% confidence level even after regressing out ENSO (Fig. S2a in the supplemental material). This is consistent with the notion that there may be other factors favoring an increase of the hemispheric extent of Antarctic sea ice.

As expected from the results shown in Fig. 12a, the SIE trends in the WP and BA sectors are not correlated with ENSO variability. This evidence that the SIE in the BA sector is not influenced by ENSO is of particular importance, because the trend here is large, negative,

and significant at 95%. One may speculate that it is due to global warming, because sea ice in the BA sector is not sensitive to ENSO. We do not, however, have enough evidence to verify this conjecture for the following two reasons. First, it is likely that the decreasing trend is at least partly enhanced by other kinds of natural variability, so this needs to be investigated. Second, the low correlation between the ENSO index and SIE in the BA sector presumably does not directly mean that sea ice in the BA sector is physically insensitive to ENSO. According to many previous studies (e.g., Simpkins et al. 2012), BA sector sea ice appears to be indeed modulated by ENSO, but when averaged over the sector, variations in the east and west halves cancel each other.

Because the relationship between ENSO and SIE changes with season (Fig. 10), the seasonal trends of SIE are also of interest. Figure S3 in the supplemental material shows the results for the same analysis but for four different seasons. The trend slope in the RS sector during the satellite era has decreased in all four seasons after regressing out ENSO variability. The ENSO removal produces the largest reduction in the trend for the NDJ season, when the trend has lost the significance as in the annual-mean analysis. This result is consistent with observational evidence that the ENSO variability is largest in austral summer. The ENSO signal in the IO sector is seen in every season except for ASO, and the

a) ENSO



b) SAM

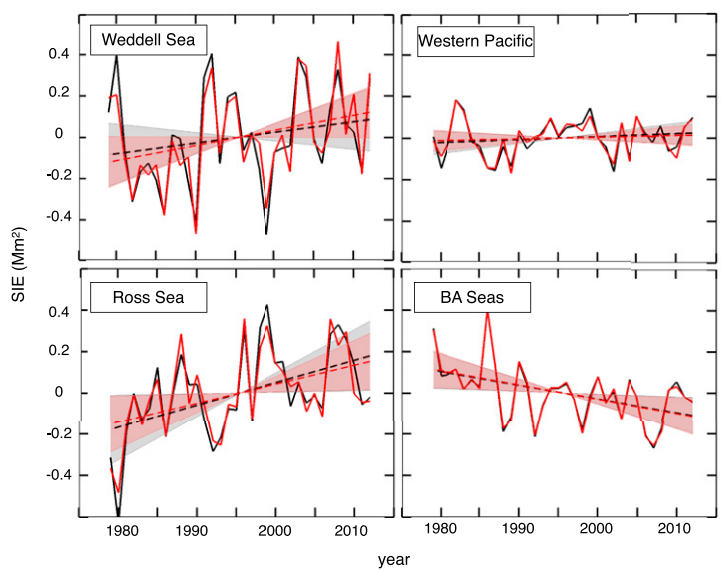
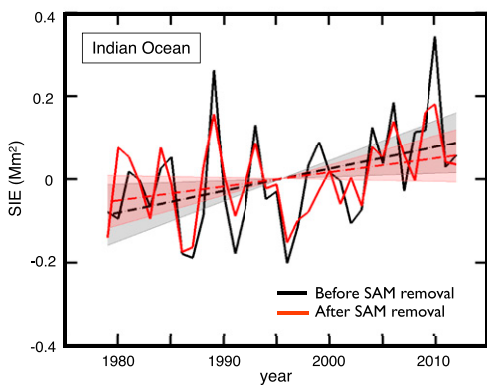


FIG. 13. (a) SIE time series for each sector before (after) regressing out the SIE variability associated with ENSO using the linear relationships shown in Fig. 12, shown in black (red) curves. Dashed lines are calculated by least squares fitting, and shaded areas show the uncertainty of the slopes at the 95% confidence level. (b) As in (a), but for SAM.

ENSO signal in the WS sector originates mostly from the NDJ season, but the trend in that season is not significant, with or without the ENSO effect included.

2) SAM

Figure 13b shows the results for SAM. We highlight the IO sector because the SIE in the IO sector exhibits the largest correlation with SAM. After regressing out SAM, the slope declines and is no longer significant at 95%. On the other hand, the positive sea ice trend in the WS sector becomes stronger after regressing out SAM, and nearly becomes significant. The other three sectors are relatively insensitive to SAM variability. As is the

case with ENSO, the positive trend of the hemispheric SIE time series retains its significance after regressing out SAM (Fig. S2b). This supports the analysis result of Simpkins et al. (2012) that the trends in sea ice over 1980–2008 are not significantly related to trends in SAM.

The seasonal analysis shown in Fig. S4 of the supplemental material suggests that the SAM signals in the IO sector mostly originate from the MJJ season, which is early winter. Therefore, this result should not be interpreted as being related to the observed SAM trend in late spring and early summer (e.g., Polvani et al. 2011), which has frequently received attention. We have further sorted the MJJ data into monthly bins and

performed the same analysis (Fig. S5 in the supplemental material). The result suggests that the SAM signal in the IO sector comes mostly from May. Hence, the SAM trend in May deserves further attention in this context.

Our results for SAM are based on the spatial pattern shown in Fig. 9, but nearly identical results are obtained even if we use the pattern extracted as the first EOF mode of unfiltered Z at 500 hPa (Fig. 2a), which is normally referred to as SAM index.

3) NPM AND DPR

We have performed the same analysis but for NPM and DPR (not shown). The sea ice responses to NPM are qualitatively similar to those of ENSO, but the influence of NPM on sea ice is weaker. The trends of annual mean sea ice in all five sectors are changed very little by regressing out either of the two indices that comprise the DPR mode. Therefore, we do not perform further analyses on NPM and DPR in this study.

c. Comparison with Holland and Kwok

Holland and Kwok (2012) showed that the trends in meteorology, especially local winds associated with sea level pressure anomalies, have expanded Antarctic sea ice during 1992–2010. We can also reproduce their trend pattern using 500-hPa Z during their time span (1992–2010; April–June) (Fig. 14a). To focus on the relationship between the trend pattern and the Rossby modes, we have repeated the same analysis as in the intraseasonal section but for strongly low-pass filtered (Fig. 4b) April–June data. In this analysis, the ENSO influence is removed using the Niño-3.4 index (i.e., the average SST anomaly over 5°S – 5°N , 170° – 120°W) for computational efficiency.

As in the previous section, the first EOF mode is the SAM pattern, and the second and third modes are Rossby wave-like modes. Figure 14b shows the second and third EOF with similar color scale and orientation to Fig. 3 of Holland and Kwok (2012). These EOF modes are calculated after removing the climatology, trend, and ENSO. Since the first mode of EOF is the SAM pattern, the Rossby modes are also not correlated with SAM.

The explained variance of these two Rossby wave-like modes are not separated by the North et al. (1982) criterion, so any linear combination of these two modes can be equally important. Therefore, in Fig. 14c, we show the trend patterns that are reconstructed from EOFs 2 and 3. Considering the similarity between Figs. 14a and 14c (spatial correlation = 0.69), the trend pattern shown in Holland and Kwok (2012) appears to be a 19-yr trend associated with Rossby wave-like modes that are orthogonal to ENSO or SAM.

Also important is that the PC time series associated with this Rossby mode does not show a significant trend

at 95% in the 34-yr record (Fig. 14d). Therefore, it is reasonable to assert that Holland and Kwok (2012) captured a fluctuation in the low-frequency variability associated with atmospheric Rossby wave-like disturbances. Even though the ultimate causes of the low-frequency modulation are equivocal, this supports the notion that the expanding Antarctic sea ice in some sectors may have resulted from stochastic variability of Earth's climate system, rather than from a long-term deterministic trend possibly resulting from climate forcing.

7. Conclusions

Our results provide a comprehensive analysis of various time and space scales of weather and climate variability and their effect on Antarctic sea ice. The main conclusions are summarized as follows.

- a. *Sea ice extent shows the largest coherence with geopotential height at 500 hPa at intraseasonal time scales with periods of 20–40 days*

Our first motivation presented in this paper is to find whether there exists a particular time scale where meteorology and sea ice are most coherent. Cross-spectral analysis clearly shows that the answer is yes: the intraseasonal time scale, between about 20 and 40 days in period, is a “sweet spot” where Z at 500 hPa explains a larger fraction of SIE variance than any other time scale. This preferred time scale is most prominent in the RS and BA sectors, but is observed at all longitudes.

- b. *Rossby waves, especially with the PSA pattern, explain a large fraction of the intraseasonal variability of the Antarctic sea ice*

To more closely examine intraseasonal variability, we have constructed a bandpass filter to focus only on the time scale for which meteorology and sea ice are most coherent. First, we perform EOF/PC analysis for bandpass filtered Z at 500 hPa to identify the spatial structure of atmospheric variability for this particular time scale. The analysis shows that quasi-stationary Rossby waves are the key phenomena in the Southern Hemisphere on this time scale.

An important point is that the Rossby modes isolated by our analysis procedure are not indicative of either ENSO or SAM, which have received much attention in the context of explaining Antarctic sea ice variability. Our analysis suggest that about 50% of the intraseasonal Antarctic SIE variance during MJJ (ice growing season) and ASO (ice maximum season) is explained by Rossby waves (especially the so-called PSA pattern) in the RS and BA sectors. During the rest of the year, Rossby

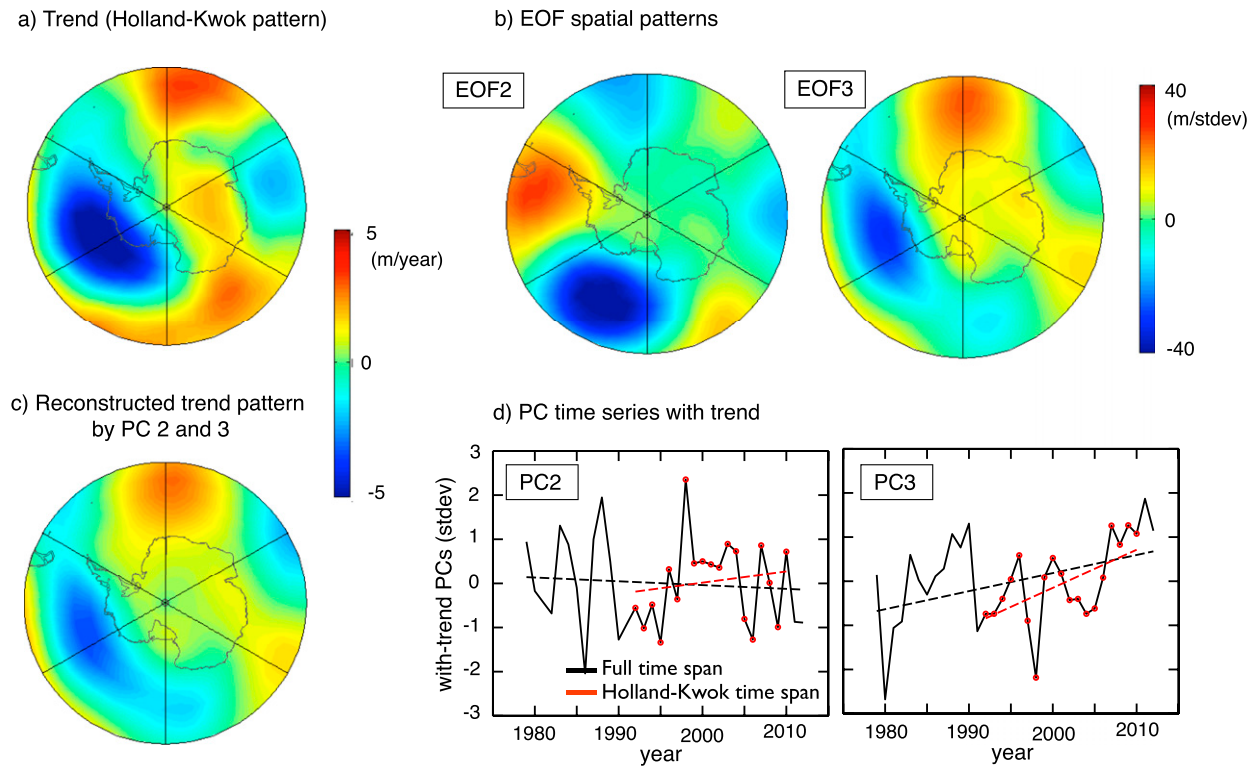


FIG. 14. (a) Linear trends of Z at 500 hPa in April–June of 1992–2010. The Greenwich meridian located on the top. (b) As in Fig. 3 but for PC2 and PC3 of strong low-pass filtered detrended data in April–June of 1979–2012. (c) Linear trends of Z at 500 hPa in April–June of 1992–2010 reconstructed by EOF2 and EOF3. (d) The time series obtained by projecting nondetrended Z onto the EOF2 and EOF3 shown in (b). Black (red) dashed line shows the least squares fitting calculated with the data of 1979–2012 (1992–2010).

waves explain about 20%, in general. Even though the SAM is not orthogonal with the Rossby modes, the spatial maps do not look like the SAM. Therefore, Rossby wave structures should receive more attention in future studies, rather than the SAM itself, at least in the intraseasonal time scale. ENSO does not influence SIE on intraseasonal time scales, because ENSO has little power in this time scale.

c. *For interannual time scales, a large amount of SIE variance is unexplained by linear relationships to ENSO and SAM, but is rather explained by a Rossby wave-like mode*

If we perform the same analysis for interannual time scales using unfiltered monthly mean data, the relative importance of climate modes on sea ice is different than that for intraseasonal variability. ENSO and SAM become more important on the interannual time scale. This is because ENSO has more power on the interannual time scale, and SAM becomes a more dominant mode of atmospheric variability. We note, however, that SIE time series cannot be explained well by a simultaneous SAM index except for Indian Ocean sector in MJJ (ice growing season). Instead, the Drake Passage Rossby (DPR) mode

explains a lot of variance in this time scale. DPR indices (PC2 and PC3) are not correlated with our ENSO nor SAM indices.

d. *In some sectors, the statistical significance of the increasing sea ice trends during the satellite era disappears after regressing out the influence of one prominent climate mode*

During the most recent three decades, some interannual climate modes have nonnegligible trends, and therefore have some implications for the increasing sea ice trend in that period. In the RS and IO sectors, if we remove the sea ice modulation associated with ENSO, then the increasing trend becomes weaker, and the statistical significance of the increasing SIE trend falls below 95%. This suggests that, at least in some sectors, after the ENSO forcing is removed, stochastic variability might be enough to explain increasing sea ice.

If the effect of SAM is removed, only the IO sectorial trend loses its significance, and the signals appear to originate mostly from May. Because both ENSO and SAM trends affect sea ice differently in different sectors, the counteraction among the WS, IO, and RS sectors makes it difficult for ENSO and SAM to explain the

increasing trend of the hemispheric total SIE during the satellite era. Since the above results are based on statistical analysis only, further physical process studies from both observational and modeling perspectives are needed.

Acknowledgments. The work was supported by the National Science Foundation (NSF) under Grant AGS-0960497 and the first author's graduate work is also supported by Takenaka Ikueikai Scholarship Society, Iizuka Takeshi Scholarship Foundation, and the NSF under Grant AGS-1122989. We are also grateful to Christopher Bretherton, Cecilia Bitz, Kyle Armour, Casey Hilgenbrink, James Renwick, and two anonymous reviewers for their helpful comments and suggestions.

REFERENCES

- Adames, Á. F., and J. M. Wallace, 2014: Three-dimensional structure and evolution of the MJO and its relation to the mean flow. *J. Atmos. Sci.*, **71**, 2007–2026, doi:[10.1175/JAS-D-13-0254.1](https://doi.org/10.1175/JAS-D-13-0254.1).
- Ainley, D. G., C. T. Tynan, and I. Stirling, 2003: Sea ice: A critical habitat for polar marine mammals and birds. *Sea Ice: An Introduction to Its Physics, Chemistry, Biology, and Geology*, D. Thomas and G. Dieckmann, Eds., Blackwell, 240–266.
- Amos, D. E., and L. H. Koopmans, 1963: Tables of the distribution of the coefficient of coherence for stationary bivariate Gaussian process. Sandia Corporation Monograph SCR-483, 328 pp.
- Ashok, K., S. K. Behera, S. A. Rao, H. Weng, and T. Yamagata, 2007: El Niño Modoki and its possible teleconnection. *J. Geophys. Res.*, **112**, C11007, doi:[10.1029/2006JC003798](https://doi.org/10.1029/2006JC003798).
- Bitz, C. M., and L. M. Polvani, 2012: Antarctic climate response to stratospheric ozone depletion in a fine resolution ocean climate model. *Geophys. Res. Lett.*, **39**, L20705, doi:[10.1029/2012GL053393](https://doi.org/10.1029/2012GL053393).
- Bretherton, C. S., M. Widmann, V. P. Dymnikov, J. M. Wallace, and I. Bladé, 1999: The effective number of spatial degrees of freedom of a time-varying field. *J. Climate*, **12**, 1990–2009, doi:[10.1175/1520-0442\(1999\)012<1990:TENOSD>2.0.CO;2](https://doi.org/10.1175/1520-0442(1999)012<1990:TENOSD>2.0.CO;2).
- Dee, D. P., and Coauthors, 2011: The ERA-Interim reanalysis: Configuration and performance of the data assimilation system. *Quart. J. Roy. Meteor. Soc.*, **137**, 553–597, doi:[10.1002/qj.828](https://doi.org/10.1002/qj.828).
- Hall, A., and M. Visbeck, 2002: Synchronous variability in the Southern Hemisphere atmosphere, sea ice, and ocean resulting from the annular mode. *J. Climate*, **15**, 3043–3057, doi:[10.1175/1520-0442\(2002\)015<3043:SVITSH>2.0.CO;2](https://doi.org/10.1175/1520-0442(2002)015<3043:SVITSH>2.0.CO;2).
- Hartmann, D. L., 2015: Pacific sea surface temperature and the winter of 2014. *Geophys. Res. Lett.*, **42**, 1894–1902, doi:[10.1002/2015GL063083](https://doi.org/10.1002/2015GL063083).
- Holland, P. R., and R. Kwok, 2012: Wind-driven trends in Antarctic sea-ice drift. *Nat. Geosci.*, **5**, 872–875, doi:[10.1038/ngeo1627](https://doi.org/10.1038/ngeo1627).
- Holton, J. R., and G. J. Hakim, 2012: *An Introduction to Dynamic Meteorology*. Academic Press, 532 pp.
- Hosking, J. S., A. Orr, G. J. Marshall, J. Turner, and T. Phillips, 2013: The influence of the Amundsen–Bellingshausen Seas low on the climate of West Antarctica and its representation in coupled climate model simulations. *J. Climate*, **26**, 6633–6648, doi:[10.1175/JCLI-D-12-00813.1](https://doi.org/10.1175/JCLI-D-12-00813.1).
- Hoskins, B. J., and D. J. Karoly, 1981: The steady linear response of a spherical atmosphere to thermal and orographic forcing. *J. Atmos. Sci.*, **38**, 1179–1196, doi:[10.1175/1520-0469\(1981\)038<1179:TSLROA>2.0.CO;2](https://doi.org/10.1175/1520-0469(1981)038<1179:TSLROA>2.0.CO;2).
- , A. J. Simmons, and D. G. Andrews, 1977: Energy dispersion in a barotropic atmosphere. *Quart. J. Roy. Meteor. Soc.*, **103**, 553–567, doi:[10.1002/qj.49710343802](https://doi.org/10.1002/qj.49710343802).
- Kao, H.-Y., and J.-Y. Yu, 2009: Contrasting eastern-Pacific and central-Pacific types of ENSO. *J. Climate*, **22**, 615–632, doi:[10.1175/2008JCLI2309.1](https://doi.org/10.1175/2008JCLI2309.1).
- Kidson, J. W., 1999: Principal modes of Southern Hemisphere low-frequency variability obtained from NCEP–NCAR reanalyses. *J. Climate*, **12**, 2808–2830, doi:[10.1175/1520-0442\(1999\)012<2808:PMOSHL>2.0.CO;2](https://doi.org/10.1175/1520-0442(1999)012<2808:PMOSHL>2.0.CO;2).
- Lefebvre, W., and H. Goosse, 2005: Influence of the southern annular mode on the sea ice–ocean system: The role of the thermal and mechanical forcing. *Ocean Sci. Discuss.*, **2**, 299–329, doi:[10.5194/osd-2-299-2005](https://doi.org/10.5194/osd-2-299-2005).
- , —, R. Timmermann, and T. Fichefet, 2004: Influence of the southern annular mode on the sea ice–ocean system. *J. Geophys. Res.*, **109**, C09005, doi:[10.1029/2004JC002403](https://doi.org/10.1029/2004JC002403).
- Li, X., D. M. Holland, E. P. Gerber, and C. Yoo, 2014: Impacts of the north and tropical Atlantic Ocean on the Antarctic Peninsula and sea ice. *Nature*, **505**, 538–542, doi:[10.1038/nature12945](https://doi.org/10.1038/nature12945).
- , E. P. Gerber, D. M. Holland, and C. Yoo, 2015a: A Rossby wave bridge from the tropical Atlantic to West Antarctica. *J. Climate*, **28**, 2256–2273, doi:[10.1175/JCLI-D-14-00450.1](https://doi.org/10.1175/JCLI-D-14-00450.1).
- , D. M. Holland, E. P. Gerber, and C. Yoo, 2015b: Rossby waves mediate impacts of tropical oceans on West Antarctic atmospheric circulation in austral winter. *J. Climate*, **28**, 8151–8164, doi:[10.1175/JCLI-D-15-0113.1](https://doi.org/10.1175/JCLI-D-15-0113.1).
- Meier, W., F. Fetterer, M. Savoie, S. Mallory, R. Duerr, and J. Stroeve, 2013: NOAA/NSIDC climate data record of passive microwave sea ice concentration, version 2. National Snow and Ice Data Center, doi:[10.7265/N55M63M1](https://doi.org/10.7265/N55M63M1).
- Mo, K. C., and R. W. Higgins, 1998: The Pacific–South American modes and tropical convection during the Southern Hemisphere winter. *Mon. Wea. Rev.*, **126**, 1581–1596, doi:[10.1175/1520-0493\(1998\)126<1581:TPSAM>2.0.CO;2](https://doi.org/10.1175/1520-0493(1998)126<1581:TPSAM>2.0.CO;2).
- North, G. R., T. L. Bell, R. F. Cahalan, and F. J. Moeng, 1982: Sampling errors in the estimation of empirical orthogonal functions. *Mon. Wea. Rev.*, **110**, 699–706, doi:[10.1175/1520-0493\(1982\)110<0699:SEITEO>2.0.CO;2](https://doi.org/10.1175/1520-0493(1982)110<0699:SEITEO>2.0.CO;2).
- Parkinson, C. L., and D. J. Cavalieri, 2012: Antarctic sea ice variability and trends, 1979–2010. *Cryosphere*, **6**, 871–880, doi:[10.5194/tc-6-871-2012](https://doi.org/10.5194/tc-6-871-2012).
- Peng, G., W. Meier, D. Scott, and M. Savoie, 2013: A long-term and reproducible passive microwave sea ice concentration data record for climate studies and monitoring. *Earth Syst. Sci. Data*, **5**, 311–318, doi:[10.5194/essd-5-311-2013](https://doi.org/10.5194/essd-5-311-2013).
- Polvani, L. M., and K. L. Smith, 2013: Can natural variability explain observed Antarctic sea ice trends? New modeling evidence from CMIP5. *Geophys. Res. Lett.*, **40**, 3195–3199, doi:[10.1002/grl.50578](https://doi.org/10.1002/grl.50578).
- , D. W. Waugh, G. J. P. Correa, and S.-W. Son, 2011: Stratospheric ozone depletion: The main driver of twentieth-century atmospheric circulation changes in the Southern Hemisphere. *J. Climate*, **24**, 795–812, doi:[10.1175/2010JCLI3772.1](https://doi.org/10.1175/2010JCLI3772.1).
- Renwick, J. A., A. Kohout, and S. Dean, 2012: Atmospheric forcing of Antarctic sea ice on intraseasonal time scales. *J. Climate*, **25**, 5962–5975, doi:[10.1175/JCLI-D-11-00423.1](https://doi.org/10.1175/JCLI-D-11-00423.1).

- Simmonds, I., and T. H. Jacka, 1995: Relationships between the interannual variability of Antarctic sea ice and the Southern Oscillation. *J. Climate*, **8**, 637–647, doi:[10.1175/1520-0442\(1995\)008<0637:RBTIVO>2.0.CO;2](https://doi.org/10.1175/1520-0442(1995)008<0637:RBTIVO>2.0.CO;2).
- Simpkins, G. R., L. M. Ciasto, D. W. J. Thompson, and M. H. England, 2012: Seasonal relationships between large-scale climate variability and Antarctic sea ice concentration. *J. Climate*, **25**, 5451–5469, doi:[10.1175/JCLI-D-11-00367.1](https://doi.org/10.1175/JCLI-D-11-00367.1).
- , S. McGregor, A. S. Taschetto, L. M. Ciasto, and M. H. England, 2014: Tropical connections to climatic change in the extratropical Southern Hemisphere: The role of Atlantic SST trends. *J. Climate*, **27**, 4923–4936, doi:[10.1175/JCLI-D-13-00615.1](https://doi.org/10.1175/JCLI-D-13-00615.1).
- Stammerjohn, S., D. G. Martinson, R. C. Smith, X. Yuan, and D. Rind, 2008: Trends in Antarctic annual sea ice retreat and advance and their relation to El Niño–Southern Oscillation and Southern Annular Mode variability. *J. Geophys. Res.*, **113**, C03S90, doi:[10.1029/2007JC004269](https://doi.org/10.1029/2007JC004269).
- Sveshnikov, A. A., 1968: *Problems in Probability Theory, Mathematical Statistics and Theory of Random Functions*. W. B. Saunders Co., 325–327 pp.
- Turner, J., and Coauthors, 2009: Non-annular atmospheric circulation change induced by stratospheric ozone depletion and its role in the recent increase of Antarctic sea ice extent. *Geophys. Res. Lett.*, **36**, L08502, doi:[10.1029/2009GL037524](https://doi.org/10.1029/2009GL037524).
- , T. Phillips, J. S. Hosking, G. J. Marshall, and A. Orr, 2013: The Amundsen Sea low. *Int. J. Climatol.*, **33**, 1818–1829, doi:[10.1002/joc.3558](https://doi.org/10.1002/joc.3558).
- Yuan, X., 2004: ENSO-related impacts on Antarctic sea ice: A synthesis of phenomenon and mechanisms. *Antarct. Sci.*, **16**, 415–425, doi:[10.1017/S0954102004002238](https://doi.org/10.1017/S0954102004002238).
- Zhang, J., 2007: Increasing Antarctic sea ice under warming atmospheric and oceanic conditions. *J. Climate*, **20**, 2515–2529, doi:[10.1175/JCLI4136.1](https://doi.org/10.1175/JCLI4136.1).